Available online at www.sciencedirect.com
ScienceDirect
Comput. Methods Appl. Mech. Engrg. 404 (2023) 115814
Computer methods in applied mechanics and engineering
www.elsevier.com/locate/cma

DEM-enriched contact approach for material point method

Hao Chen[a], Shiwei Zhao[b,*], Jidong Zhao[b,c], Xiaowen Zhou[a]

[a] State Key Laboratory of Subtropical Building Science, South China University of Technology, Guangzhou, China
[b] Department of Civil and Environmental Engineering, The Hong Kong University of Science and Technology, Hong Kong Special Administrative Region of China
[c] HKUST Shenzhen-Hong Kong Collaborative Innovation Research Institute, Futian, Shenzhen, China

Received 21 July 2022; received in revised form 19 November 2022; accepted 22 November 2022
Available online 9 December 2022

Abstract

A major challenge for material point method (MPM) is to model multi-body and multi-material interactions. Prevailing contact schemes developed for MPM suffer from numerical instabilities, especially for the coexistence of multiple material boundary conditions. This study proposes a generalized contact scheme based on a hybrid scheme of MPM and discrete element method (DEM) to tackle such issues. The new scheme contains two novel features of particle–particle and particle–structure contact schemes guided by a DEM contact model to handle multi-material interactions. It leverages the advantages of both MPM and DEM, offering a unified way to flexibly handle either the boundary–particle or particle–particle multi-material interactions. Several typical physical processes are simulated to showcase the versatility of the proposed approach, including interface rotation and sliding, penetration, and granular material impact. It demonstrates that the generalized contact scheme can flexibly capture the mechanical responses of multi-body and multi-material systems in MPM.

Keywords: Contact algorithm; Material point method; Discrete element method; Penalty method; Granular material

1. Introduction

Material point method (MPM) [1,2] is a promising mesh-free approach for tackling large deformation problems. It serves as an effective alternative to the traditional finite element method (FEM) which often encounters the mesh distortion issue when the material reaches the large-deformation regime. Some improvements have been reported in mitigating the mesh entanglement of FEM, such as Arbitrary Lagrangian–Eulerian (ALE) [3], Remeshing and Interpolation Technique with Small Strain (RITSS) [4,5] and Particle Finite Element Method (PFEM) [6]. However, these remedy measures are frequently accompanied with trade offs such as increased computational cost and convergence issues [7]. MPM has gained increasing attractions for solving practical engineering problems involving large deformation, e.g., dynamic compaction [8,9], penetration and pile installation [10,11], landslide [12,13] and debris flow impacting [14,15] or even solid–liquid interaction [16]. In MPM, the continuum domain is represented by a cluster of material points (Lagrangian description) assigned with all the physical properties (e.g., mass, momentum, strain and stress). The solution domain characterized by the fixed background mesh (Eulerian description) serves

* Corresponding author.
E-mail address: ceswzhao@ust.hk (S. Zhao).

https://doi.org/10.1016/j.cma.2022.115814
0045-7825/

as momentum equation integration padding and carries no permanent mechanical information. State variables are mapped back and forth between the material points and the background nodes, bypassing any update of mesh topology in FEM. Moreover, MPM is sensitive to the shape function that establishes the relationship between the material points and the nodes. The primitive version of MPM proposed by Sulsky et al. [1] suffers from the cell crossing noise. To fix the numerical artefacts from the cell crossing, Bardenhagen and Kober [17] advanced the MPM with the Generalized Interpolation Material Point method (GIMP), which is the MPM version employed in this study.

In addition to tackling large-deformation problems, MPM enables the treatment of multi-material interaction in a natural manner using its built-in penetration constraint. However, the penetration constraint fails to handle the free separation condition for two different materials, which sometimes can cause inaccurate results, e.g., much higher resistance in penetration problems [2]. The literature has reported the augmented one-step MPM contact algorithm following the Coulomb friction criterion [18] and the free separation criterion [19]. Since the additional dynamic update of nodes on account of the one-step contact algorithm occurring on the deformed grid, the consistency of nodal properties cannot be guaranteed between the current timestep (deformed grid) and the subsequent timestep (resetting grid). Therefore, the one-step contact algorithm does not provide a rigorous velocity correction for contact models like the Coulomb friction model. Huang et al. [20] presented a twice-correct-one-timestep strategy for the contact algorithm. The velocity correction is performed on deformed and redefined grids to assure a precise no-penetration condition. Notably, all these contact algorithms summarized above are node-wise. In other words, the instabilities of these methods can be associated with the indirect physical properties manipulation. The extrapolated mass, momentum and force are fed to the contact calculation and the contact criterion determination occurs on the background grid. Concerning the precision of the grid-based contact algorithm, Nairn et al. [21] not only implemented a similar twice-correct-one-step scheme as Huang et al. [20], but put forward a Logistic Regression method (LR) seeking for more truthful contact normal computation. For nodes linking to more than one material field, the *Point Clouds* consisting of the neighboring material points around these nodes are defined and assist the separate normal for potential contact materials based on the Support Vector Machine algorithm. The obtained separate normal is taken as the contact normal. To some extent, the LR method can be regarded as an optimized way of finding contact normal statistically compared to the traditional contact normal computation using the extrapolation of mass gradient [18] or volume gradient [22]. Nevertheless, the robustness of the LR method remains an open issue when the stiffness between the interacted materials varies dramatically. The obtained contact force can be under-estimated due to an inappropriate material inter-penetration [23].

The discrete element method (DEM), long known for its predominant role in dealing with the interaction of massive individual particles, has been attempted to work with the MPM in tackling macroscopic multi-body problems. Liu et al. [24] implemented a contact algorithm by coupling the MPM and DEM to model the impact between collapsing sand and the wooden blocks. In this approach, MPM predicts the behavior of the sand, while shrunken-point DEM characterizes the motion of the blocks. Virtual material points are attached to the corners and edges of the DEM block to bridge the kinematics between MPM and DEM solver. The contact algorithm of Liu et al. [24] can be viewed as a DEM-assisted node-wise contact algorithm as it offers an advantage in coping with the interaction between two materials with highly different stiffness. Even though the results of Liu et al. [24] show excellent agreement with experimental results, the contact detection still follows the traditional MPM contact rules since the contact state is governed by the approaching velocity of virtual material points. It indicates that method Liu et al. [24] does not escape the drawbacks of the velocity check criterion [25] in the conventional MPM framework. Under the same MPM-DEM model, Jiang et al. [26] put forth a Material Point-Spheropolygon-Discrete Element Method (MPM-SDEM) to avoid the shortcoming of the velocity criterion for nodal contact detection. This hybrid scheme replaces the DEM block surrounding the virtual material points with a SDEM shape deduced by the Minkowski sum of polygon and disk. Interactions between the material points and the SDEM shape follow the DEM contact model and overcome the grid-dependency weakness in Liu et al. [24]. A similar penalty method is also reported by Guilkey et al. [27], which pays attention to the contact between the material points and the rigid parts with complex shapes. Line segments or triangular surfaces are introduced to demonstrate a rigid block with an irregular shape. Though following the same way of acquiring force through penalty function as Jiang et al. [26], the contact advection of Guilkey et al. [27] is different. Guilkey et al. [27] passes the obtained contact force to the nodes in an interpolation manner instead of considering the contact force as the body force of the material points straightforwardly. Note that the method of Guilkey et al. [27] has a trade-off by increasing the computational cost

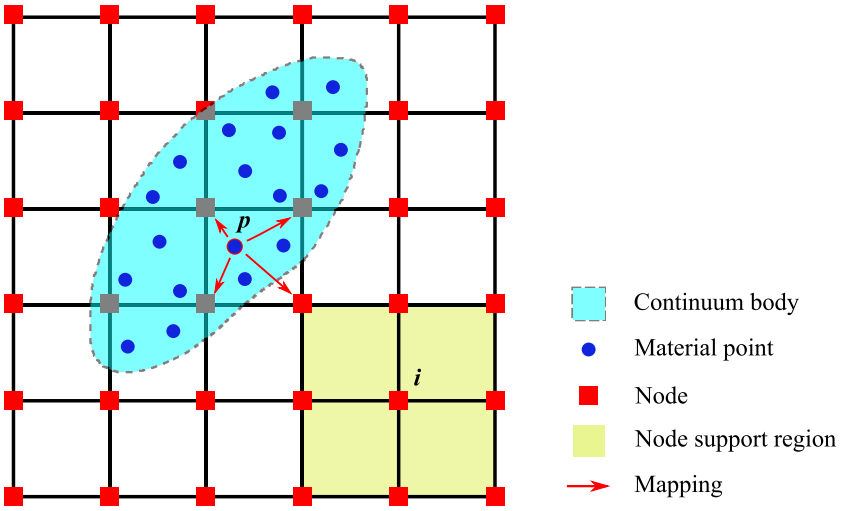

Fig. 1. Schematic diagram of the hybrid description of the MPM. (For interpretation of the references to color in this figure legend, the reader is referred to the web version of this article.)

in terms of the massive intersection detection between the geometry components. In this case, the domain has to be discretized sufficiently fine to approximate a solution region accurately. Jiang et al. [28] enhanced the existed coupled MP-DEM algorithm for modeling the penetration of the solid intruder. Within the framework of Jiang et al. [28], the balance between the computational cost and the simulation precision is reached by introducing the disk–disk coupling scheme under the simplified particle shape condition (both material point and DEM particle are assumed as the disk in 2D). Such an elegant coupling scheme helps avoid the internal deficiency of the grid-based contact algorithm of MPM without imposing too much additional simulation complexity. It captures the mechanism underlying the collision between complex shapes intuitively.

To sum up, the literature illustrates the node-based contact algorithm and the DEM-assisted contact correction. The first method inherits the natural feature of MPM but may suffer from a precision loss in modeling the material with significant stiffness differences. The latter is mainly found in the MP-DEM format regarding the penalty function and shows promising potential in contact algorithms with complicated boundary conditions. In this work, a generalized contact approach is proposed based on an MP-DEM framework. The novel contact scheme has two variations, i.e., rigid–nonrigid and nonrigid–nonrigid contact schemes, where the rigid–nonrigid one is for two different materials and additional boundary conditions, while the nonrigid–nonrigid one is dedicated to more general interaction between material-point clusters with irregular shapes. Moreover, the proposed contact algorithm is applicable to various contact models (linear-spring or plastic contact model), an abundance of particle shapes (e.g., disk, polygon and sphero-polygon). Meanwhile, contact force can be flexibly applied either through nodes or on material points directly, conditioned on a trade-off between simulation accuracy and efficiency.

2. Material point method

MPM, as a numerical technique for the continuum, can be formulated based on the principle of virtual work as often implemented in FEM. Unlike FEM, MPM has both Lagrangian and Eulerian components for spatial discretization. As illustrated in Fig. 1, the continuum domain is discretized into a finite number of material points (Lagrangian components) which carry all the physical properties. Meanwhile, the support region (in yellow) determines the mapping relationship between material points and nodes (Eulerian components). At the beginning of each MPM computational cycle, the kinematics information of material points will be extrapolated into the initialized background grid, where the momentum equation is solved. The solution (the dynamics of the nodes) will then be interpolated back to the material points for updating the corresponding state variables.

2.1. Governing equations

The balance equation of linear momentum reads as:

$$\rho \boldsymbol{a} = \nabla \cdot \boldsymbol{\sigma} + \rho \boldsymbol{b} \tag{1}$$

where $\boldsymbol{a}$ is the acceleration term, $\boldsymbol{\sigma}$ is the Cauchy stress tensor, ρ is the density and $\boldsymbol{b}$ is body force per unit of mass performed on materials. Introducing virtual displacement vector $\delta \boldsymbol{u}$ and integrating the Eq. (1) over the solution domain Ω, one gets the weak form:

$$\int_{\Omega} \rho \boldsymbol{a} \cdot \delta \boldsymbol{u} dV = \int_{\Omega} \rho \boldsymbol{b} \cdot \delta \boldsymbol{u} dV + \int_{\partial \Omega} \boldsymbol{\tau} \cdot \delta \boldsymbol{u} dS - \int_{\Omega} \boldsymbol{\sigma} \cdot \nabla \delta \boldsymbol{u} dV \tag{2}$$

where $\boldsymbol{\tau} = \boldsymbol{\sigma} \cdot \boldsymbol{n}$ is the surface traction applied on the material boundary and $\boldsymbol{n}$ is the outward unit normal of the material boundary surface at the current configuration.

The original version of MPM proposed by Sulsky et al. [1] extrapolates material density by:

$$\rho(\mathbf{x}, t) = \sum\nolimits_p m_p \delta(\mathbf{x} - \mathbf{x}_p) \tag{3}$$

where m_p is the mass of the specific material point, δ is the Dirac delta function and $\mathbf{x}_p$ is the position vector of the material point.

To minimize the numerical instability caused by the Dirac delta function when cell-crossing happens, GIMP is adopted to deduce the weak form:

$$\begin{aligned} \sum_p \int_{\Omega_p \cap \Omega} \frac{\dot{\boldsymbol{p}}_p}{V_p} \chi_p(\mathbf{x}) \cdot \delta \boldsymbol{u} dV = & \sum_p \int_{\Omega_p \cap \Omega} \frac{\boldsymbol{m}_p}{V_p} \chi_p(\mathbf{x}) \boldsymbol{b}_p \cdot \delta \boldsymbol{u} dV \\ & + \sum_p \int_{\partial \Omega_\tau} \boldsymbol{\tau} \cdot \delta \boldsymbol{u} dS - \sum_p \int_{\Omega_p \cap \Omega} \boldsymbol{\sigma}_p \chi_p(\mathbf{x}) \cdot \nabla \delta \boldsymbol{u} dV \end{aligned} \tag{4}$$

where $\dot{\boldsymbol{p}}_p = m_p \dot{\boldsymbol{v}}_p$ is the derivative of the momentum of material points with respect to time and $V_p = \int_{\Omega_p \cap \Omega} \chi_p(\mathbf{x}) dV$ is the volume of a material point.

2.2. Spatial discretization and dynamics update

The virtual displacement can be interpolated in terms of the nodal shape function, given by:

$$\delta \boldsymbol{u} = \sum_i \delta \boldsymbol{u}_i N_i(\mathbf{x}) \tag{5}$$

where the discrete sum is over all the nodes owning a non-zero shape function to the given position vector $\mathbf{x}$; $\delta \boldsymbol{u}_i$ is the virtual displacement of the ith node, and $N_i(\mathbf{x})$ is the shape function value that the ith node contributes to the given point at $\mathbf{x}$.

Substitution of Eq. (5) into Eq. (4) leads to the following discrete form for the balance equation of momentum:

$$\sum_p S_{ip} \frac{d \boldsymbol{p}_p}{dt} = \boldsymbol{f}_{i,ext} + \boldsymbol{f}_{i,int} \tag{6}$$

where,

$$\boldsymbol{f}_{i,int} = -\sum_p V_p \boldsymbol{\sigma}_p \cdot G_{ip} \tag{7a}$$

$$\boldsymbol{f}_{i,ext} = \sum_p m_p \boldsymbol{b}_p S_{ip} + \int_{\partial \Omega_\tau} \boldsymbol{\tau} N_i dS \tag{7b}$$

Note that the $\boldsymbol{f}_{i,ext}$ denotes the external loads applied on the solution domain, integrated from body force and boundary surface traction force; $\boldsymbol{f}_{i,int}$ denotes the internal loads. The nodal dynamics update can be rewritten as:

$$\boldsymbol{p}_i^{(n+1)} = \boldsymbol{p}_i^{(n)} + \boldsymbol{f}_i^{(n)} \Delta t \tag{8a}$$

$$\boldsymbol{f}_i^{(n)} = \boldsymbol{f}_{i,ext}^{(n)} + \boldsymbol{f}_{i,int}^{(n)} \tag{8b}$$

$$\boldsymbol{p}_i^{(n)} = \sum_p \boldsymbol{p}_p^{(n)} S_{ip}^{(n)} \tag{8c}$$

$$\boldsymbol{m}_i^{(n)} = \sum_p \boldsymbol{m}_p^{(n)} S_{ip}^{(n)} \tag{8d}$$

Three different shape function representations are introduced in Eqs. (7) and (8), where N_i is the original hat nodal shape function, and S_{ip} and G_{ip} are generalized interpolation shape function and generalized interpolation gradient shape function, respectively, defined as

$$S_{ip} = \frac{1}{V_p} \int_{\Omega_p \cap \Omega} \chi_p(\mathbf{x}) N_i(\mathbf{x}) dV \tag{9a}$$

$$G_{ip} = \frac{1}{V_p} \int_{\Omega_p \cap \Omega} \chi_p(\mathbf{x}) \nabla N_i(\mathbf{x}) dV \tag{9b}$$

2.3. Kinematics update

The FLIP [29] and PIC [30] methods are commonly adopted to update particle velocity $\boldsymbol{V}$ in MPM, i.e.,

$$\boldsymbol{V}^{n+1} = \boldsymbol{V}^n + S\boldsymbol{a}\Delta t \qquad \text{FLIP} \tag{10a}$$

$$\boldsymbol{V}^{n+1} = S\boldsymbol{v}^{n+1} \qquad \text{PIC} \tag{10b}$$

where a variable with a superscript n or $n+1$ is referred to the corresponding variable at timestep n or $n+1$ hereafter; $\boldsymbol{v}$ and $\boldsymbol{a}$ are the nodal velocity and acceleration, respectively; S denotes the shape function matrix for interpolating dynamics from nodes to material points.

The combined velocity and position update scheme is:

$$\boldsymbol{V}^{n+1} = (1-\beta)[\boldsymbol{V}^n + S\boldsymbol{a}\Delta t] + \beta S\boldsymbol{v}^{n+1} \tag{11a}$$

$$\mathbf{x}^{n+1} = \mathbf{x}^n + \boldsymbol{v}^{n+\frac{1}{2}}\Delta t - 0.5\beta(\boldsymbol{V}^n - \boldsymbol{v}^{\mathbf{n}})\Delta t \tag{11b}$$

where $\boldsymbol{x}$ is the position of a material point; β is the so-called PIC fraction with a value between 0 and 1. A total PIC scheme is applied for $\beta = 1$, whilst a total FLIP scheme for $\beta = 0$. PIC is beneficial for enhancing numerical stability but may introduce excess damping, while FLIP conserves the physical states as much as possible but causes fictitious oscillations, especially in stress. The combined kinematics update is a compromise between the numerical noise and the artificial damping.

For some engineering problems demanding a higher resolution of results, the mixed FLIP and PIC method is inadequate for performance improvement due to the inherent pitfall of MPM relating to the error accumulation caused by the degree of freedom (DOF) mismatch between material points and the nodes. Specifically, the interpolation from nodes to material points is based on the mapping matrix (S) with dimensions of $N \times n$, where N for the DOFs of material points and n for the DOFs of nodes. One may need the inverse matrix of S to extrapolate the state variables from material points to the nodes. In terms of the non-square S, the weighted least square method is introduced by Sulsky et al. [1] to form a pseudo-inverse matrix of S, which is denoted by $S^+ = (S^T M)^{-1} S^T diag(M)$, where M is the vector of material points mass. Nonetheless, the literature [31,32] reported that the accuracy of the approximate solution (S^+) could not be guaranteed when the difference between the material points and nodes DOFs is dramatic. Therefore, the XPIC engine proposed by Hammerquist and Nairn [31] is periodically executed to diminish the numerical error. The XPIC iteration scheme is as follows:

$$\boldsymbol{V}^{n+1} = [\mathbf{I} - (\mathbf{I} - SS^+)^m]\boldsymbol{V}^n + S\boldsymbol{a}\Delta t \tag{12a}$$

$$\mathbf{x}^{n+1} = \mathbf{x}^n + S\boldsymbol{v}^n\Delta t + 0.5(\boldsymbol{V}^{n+1} - \boldsymbol{V}^n)\Delta t \tag{12b}$$

where the superscript m denotes the order of the XPIC ranging from 1 to the $+\infty$; S^+ denotes the shape function matrix for extrapolating dynamics from material points to nodes. PIC can be viewed as a particular case of XPIC with $m = 1$. When m approaches the infinite, it can be stated that the MPM iteration eliminates the numerical oscillation significantly without introducing too much damping.

2.4. Constitutive material model

Granular materials such as soils have non-linear and history-dependent mechanical responses. The literature has reported extensive constitutive models to reflect the complicated relationship between stress and strain. For simplicity, the classical Mohr–Coulomb model and the Drucker–Prager model are introduced here to demonstrate the elastoplastic behavior of soils.

The yield surface and flow rule of the Mohr–Coulomb are identical to that of Menetrey and Willam [33], and the yield function is given by:

$$F = R_{mc} q - p \tan\phi - c \tag{13a}$$

$$R_{mc}(\Theta, \phi) = \frac{1}{\sqrt{3}\cos\phi} \sin(\Theta + \frac{\pi}{3}) + \frac{1}{3} \cos(\Theta + \frac{\pi}{3}) \tan\phi \tag{13b}$$

where p and q are the mean stress and deviatoric stress, respectively; ϕ and c are the friction angle and cohesion strength, respectively; Θ is the Lode angle.

The flow rule of the Mohr–Coulomb is given by:

$$G = \sqrt{(\epsilon c|_0 \tan\psi)^2 + (R_{mw} q)^2} - p \tan\psi \tag{14a}$$

$$R_{mw}(\Theta, e) = \frac{4(1-e^2)\cos^2\Theta + (2e-1)^2}{2(1-e)^2\cos\Theta + (2e-1)\sqrt{4(1-e^2)\cos^2\Theta + 5e^2 - 4e}} R_{mc}(\frac{\pi}{3}, \phi) \tag{14b}$$

$$R_{mc}(\frac{\pi}{3}, \phi) = \frac{3 - \sin\phi}{6\cos\phi} \tag{14c}$$

where ϵ and e are parameters for the flow rule curve determination, and ψ denotes the dilation angle.

The yield function and flow rule of the Drucker–Prager model [34] are similar to that of the Mohr–Coulomb model, and the principal stresses are replaced by the von Mises stress and the spherical stress as:

$$F = \sqrt{J_2} + \eta \sigma_m - \xi c \tag{15a}$$

$$G = \sqrt{J_2} + \bar{\eta} \sigma_m \tag{15b}$$

where the J_2 is the second invariant of deviatoric stress tensor, σ_m is the spherical stress, c is the cohesion strength; η, ξ and $\bar{\xi}$ can be obtained by the friction angle (ϕ) and dilation angle (ψ),

$$\eta = \frac{3\tan\phi}{\sqrt{9 + 12\tan^2\phi}} \tag{16a}$$

$$\xi = \frac{3}{\sqrt{9 + 12\tan^2\phi}} \tag{16b}$$

$$\bar{\eta} = \frac{3\tan\psi}{\sqrt{9 + 12\tan^2\psi}} \tag{16c}$$

In terms of the tension cut-off, the yield function and flow of Drucker–Prager model is given as:

$$F = \sigma_m - \sigma_t \tag{17a}$$

$$G = \sigma_m \tag{17b}$$

where σ_t is the tension cut-off strength.

3. Discrete-element-based contact approach

3.1. An MP-DEM contact framework

Traditional MPM contact algorithm handles the material collision aided by the information mapped on the background grid from material points. In other words, the nodes are fully responsible for the boolean contact state and the geometry/physics determination of potential contact for particle pairs. Approaching velocities mapped on the same node from different material fields claim an existed contact. Furthermore, the corresponding contact normal is determined by extrapolating the mass gradient or volume gradient of material points. However, the satisfaction

of the velocity contact criterion is necessary but not sufficient. Early contact may happen in advanced interpolation algorithms such as B-SPLINE or GIMP for material points whose shape functions share the same node, even though their positions are one more cell far away. Moreover, the contact normal calculation is still an open issue for traditional contact algorithms. Whatever contact normal stands on the mass/volume gradient or more advanced Level Set Based algorithm [35], the contact normal resolution depends on the grid and material point clouds topology. One may expect that the contact normal cannot be analytically obtained for non-uniformly distributed material points. Some emerging material point-discrete element method (MP-DEM) contact algorithms have been proposed and developed to overcome the inherent defects of the grid-based contact algorithm relating to contact detection and normal calculation. It can be found that almost all of these MP-DEM contact algorithms emphasize the interaction between the rigid boundary condition carrier (e.g., penetrator or intruder) and the non-rigid materials. Moreover, the rigid bodies are always regarded as either DEM blocks with simple shapes (e.g., spheres) or sampled by intensive rigid material points. The former assumption neglects the shape variation, including irregular convex and concave, while the latter does not escape from the node-directed contact algorithm scheme in practice, as the contact state variable mapping between rigid and non-rigid material points is inevitable.

Inspired by the previous studies, a contact algorithm within the MP-DEM contact algorithm framework is proposed here. Inheriting the basic features of the rigid boundary condition-orientation MP-DEM contact algorithms, this contact algorithm is further extended to a more generalized contact solver. Two main aspects are included in this novel contact algorithm: one for rigid–nonrigid material interaction and the other for nonrigid–nonrigid collision. The first component satisfies the interaction demand between the granular materials and the geo-structures. In contrast, nonrigid–nonrigid contact focuses on the general purpose of the communication between materials without any boundary conditions. Note that the DEM contact engine drives the core of this algorithm. Not only the trivial disk–disk contact handler is implemented, but the GJK algorithm is introduced for the complex shape contact detection. The flexible transfer between the material points and DEM particles allows the contact normal and contact penetration can be acquired analytically instead of interpolating. Though we adopt the linear spring contact model to identify the force–displacement relationship between contact pairs for efficiency, an advanced contact model aiming at the non-linear mechanical behavior of material (e.g., viscous or plastic contact model) can be brought in naturally. Compared to the previous MP-DEM algorithms, this framework provides two options for the force exchange between the MPM and DEM phases. Contact force can be applied to the target particles through node-mapped or body force, and the trade-off between computational accuracy and efficiency can be achieved more straightforwardly. The detailed of this contact algorithm is described as follows.

The MPM calculation cycle considering the rigid–nonrigid contact is summarized in Algorithm 1.

Algorithm 1: Pseudocode of MPM with the proposed rigid–nonrigid contact algorithm.

```
foreach timestep do
    Background nodes dynamics reset.
    Boundary condition imposition.
    if rigid-nonrigid contact then
        if n%iterperioid == 0 then
            //(n for current step, iterperiod for neighbor list update period);
            update the rigid block neighbor list;
        end
        contact detection;
        project the contact force to the background nodes.
    end
    Project the mass and momentum from material points to nodes.
    Update the strain and stress of material points.
    Calculate the nodal force including: external force, internal force and contact force.
    Update the nodal momentum.
    Update the velocity and position of material points.
end
```

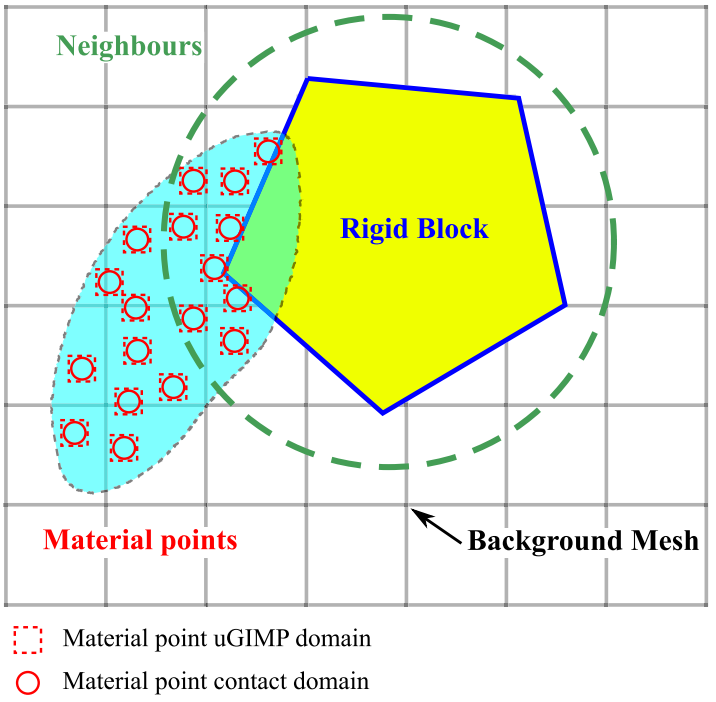

Fig. 2. Rigid–nonrigid contact model: Schematic diagram for the rigid block and the domain of non-rigid material points.

3.2. Rigid-nonrigid contact

3.2.1. Broad phase contact detection

Rigid material points are commonly employed in rigid boundaries. The rigid–nonrigid contact algorithm corrects the kinematics of the nonrigid material points only and leaves the rigid material points with boundary condition settings. Fig. 2 illustrates the interaction between a rigid block and a continuum occupied by material points. The rigid block will always maintain its neighbor list, saving the position vector of material points within a certain distance (dash green line). The cached neighbor list of nonrigid material points will be updated every specific step to avoid an intensive computational overhead. In each timestep, the material points in the neighbor list will be regarded as contact pair candidates and looped by the contact algorithm for further contact force calculation. Subsequently, all the forces applied on the material points, such as external force, internal force and the contact force, will be merged into nodes.

3.2.2. Accurate contact detection and contact force calculation

Fig. 3 illustrates a contact pair between a material point (O_A) and a rigid block (O_B). The intersection geometry is depicted by the Gilbert–Johnson–Keerthi (GJK) algorithm [36], which is widely applied in contact detection for convex shapes. Moreover, the GJK-enhanced contact algorithm in this study is expected to offer the possibility of mimicking the interaction between material point clusters and rigid blocks with convex shapes. Specifically, as illustrated in Fig. 3, the contact penetration geometry calculated by the GJK algorithm is represented by the green line and the penetration depth is denoted by δ. Following the force–displacement law, the contact force applied on the material point can be determined by δ and the relative velocity between the O_A and O_B (Eq. (18)). Note that the penetration δ can be area in 2D (gray region in Fig. 3) or volume in 3D except the classic penetration depth (green line in Fig. 3), while the corresponding contact stiffness will be area- and volume-related, respectively.

$$\boldsymbol{f}_n^{n+1} = k_n \delta \cdot \boldsymbol{n} \tag{18a}$$

$$\boldsymbol{f}_t^{n+1} = \min(\boldsymbol{f}_t^n + \Delta \boldsymbol{f}_t, \mu \| \boldsymbol{f}_n^{n+1} \|) \tag{18b}$$

$$\Delta \boldsymbol{f}_t = k_t \Delta \boldsymbol{u} \tag{18c}$$

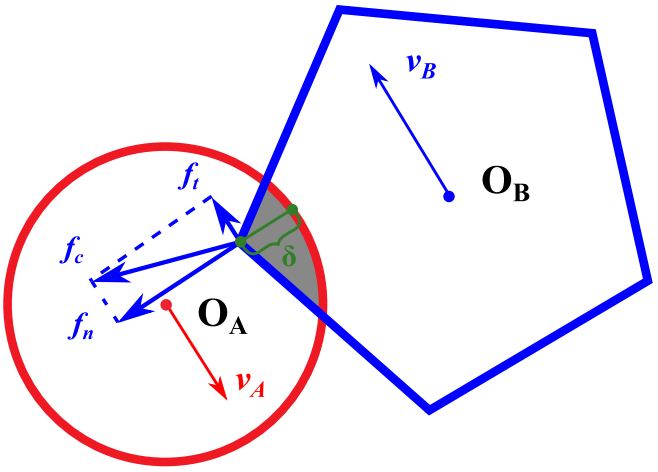

Fig. 3. Rigid–nonrigid contact model: Contact law execution between rigid block and the target non-rigid material point. (For interpretation of the references to color in this figure legend, the reader is referred to the web version of this article.)

$$\Delta \boldsymbol{u} = (\boldsymbol{v}_A - \boldsymbol{v}_B)\Delta t - [(\boldsymbol{v}_A - \boldsymbol{v}_B) \cdot \boldsymbol{n}]\boldsymbol{n}\Delta t \tag{18d}$$

where $\boldsymbol{f}_n^{n+1}$ is the normal contact force at step $n+1$; $\boldsymbol{f}_t^{n+1}$ and $\boldsymbol{f}_t^n$ are tangential forces at step $n+1$ and n, respectively; δ can be the penetration depth, area for 2D or volume for 3D; $\boldsymbol{n}$ is the contact normal pointing from O_B to O_A; $\Delta \boldsymbol{f}_t$ is the incremental tangential force; $\Delta \boldsymbol{u}$ is the relative tangential displacement between O_A and O_B; $\boldsymbol{v}$ for velocity and Δt for time step; k_n, k_t denote the normal and tangential contact stiffness and μ denotes the friction coefficient.

3.2.3. *Contact force imposition on material points*

The contact force imposition is a crucial component for evaluating the robustness of the contact algorithm. Possible contact force forms are body force and traction force. Contact force being accounted as body force (external force) of material points is efficient and does not need additional force mapping from the particle edge to the nodes. However, force mapping is necessary for the contact force regarded as traction force, and an integration term pertains to the mapping process. Hence, a more precise result can be expected. It should be pointed out that the square with a dashed line and the circle domain (Fig. 4) play a divergent role in the force acquirement. The dashed square denotes the uniform generalized interpolation material point domain (uGIMP), which contributes to the properties mapping between the Lagrangian and Eulerian phases but not for the contact detection. In contrast, the circle domain has nothing to do with the shape function determination but serves as the geometrical shape for the DEM contact model. The details of the force imposition are as follows:

- Contact force is split into sub-force components distributed uniformly on the material points edge close to the contact side. As the springboard of the force transmission, nodes help to interpolate the space continuous contact force to the traction force of material points, as presented in Fig. 4.
- Vector of the contact force initializes the integral surface configuration in the direction of the contact force. In this way, the contact force can be equivalent to the sets of forces components ($f_{ci} = \frac{f_c}{(i-1)}$ marked by the blue arrow) that applied on the material point domain edge. The resolution of the integration scheme is denoted by the subscript i, while the integration segment is illustrated by p_i. It can be observed that a higher i signifies a more accurate result correspondingly. For example, Fig. 4 takes integration resolution as $i = 5$. Therefore, force that applied on the p_i is $f_{ci} = 0.25 f_c,\ \forall i \in (1, 4)$.
- Force components will be extrapolated to the activated green nodes, which share the non-zero shape function with each integration segment (p_i). One may see that the activated nodes may not be identical to those activated by the GIMP shape function. An optimal value is introduced to shrink the integration area to eliminate the numerical oscillation caused by the discrepancy of the nodes. As a result, the contact activated node can converge to the uGIMP domain activated nodes. The value to scale the integration area is an open issue and is recommended as the $\sqrt{2}/2$ here.

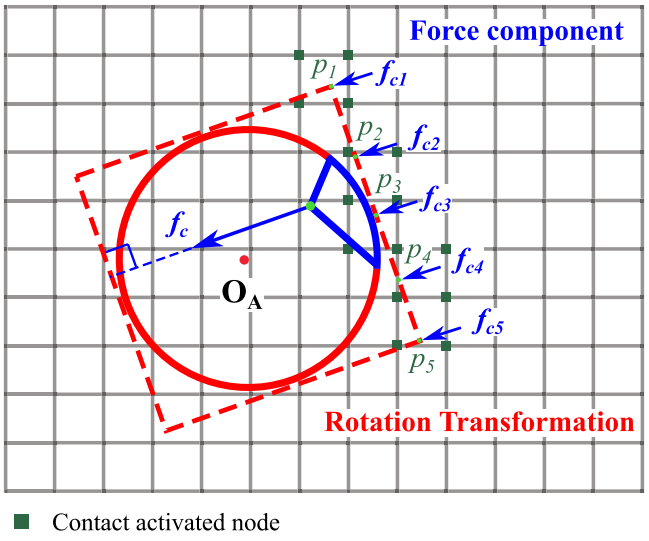

Fig. 4. Rigid–nonrigid contact model: Contact force imposition on the target material point. (For interpretation of the references to color in this figure legend, the reader is referred to the web version of this article.)

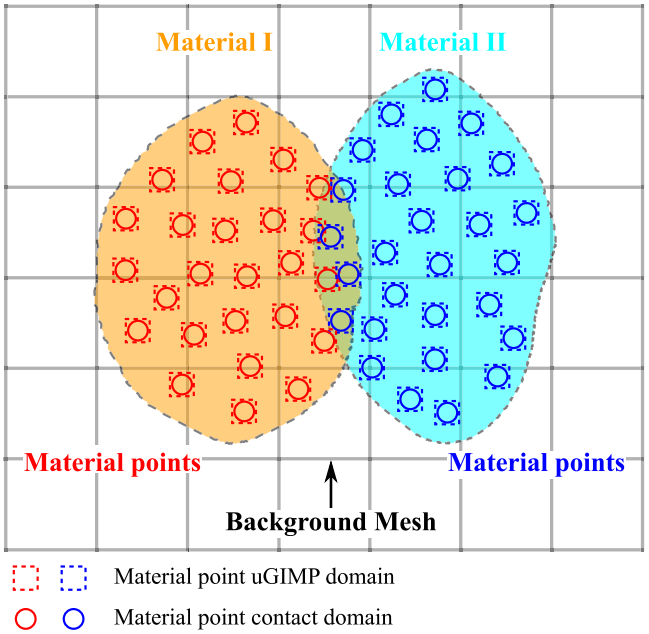

Fig. 5. Nonrigid–nonrigid contact model: Schematic diagram for the domain of material point pair.

3.3. Nonrigid-nonrigid contact

3.3.1. Kinematics mapping on the multi-layer grid

A nonrigid–nonrigid contact algorithm is proposed and is expected to collaborate with the rigid–nonrigid contact algorithm for generalized contact condition handling. Unlike the rigid–nonrigid contact algorithm in Section 3.2, two material types will be involved in the nonrigid–nonrigid algorithm. Fig. 5 exemplifies the instant contact configuration of two materials touching each other. One-layer background mesh is extended to multi-layers at the moment of contact emerging to track the physical properties exchange between different material types [37].

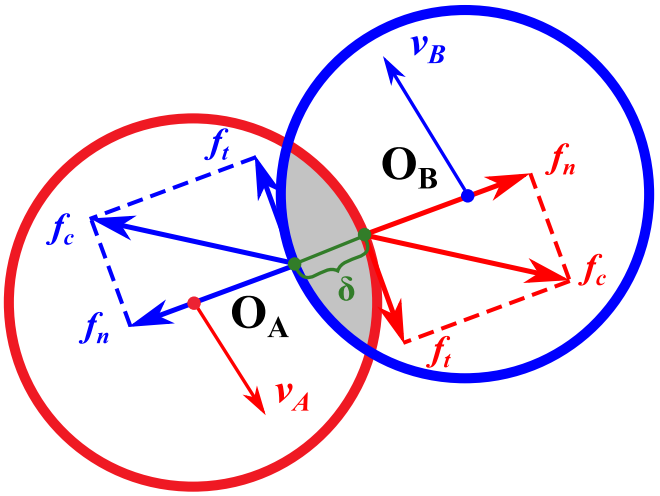

Fig. 6. Nonrigid–nonrigid contact model: Contact law execution between two material points whose shapes are assumed to be disk.

The kinematics extrapolation from material points to the nodes with multiple layers has been finished prior to the nonrigid contact detection. Each material type will independently carry out its particle-to-node mapping and material kinematics convection.

3.3.2. Contact law for material point pairs

The nonrigid–nonrigid contact algorithm rather than the MPM internal anti-penetration correction will take over the execution of multi-material interaction, aiming to avoid the over-contact numerical oscillation. Meanwhile, the algorithm allows multi-material contact modes for more than two materials, thanks to the easy extension of the node layer from two to any given number. Note that the contact algorithm execution will not loop over all the nodes but those with more than two layers activated. Moreover, the constitutive model of the nonrigid–nonrigid contact for the activated nodes is similar to that of the rigid–nonrigid contact algorithm, as shown in Fig. 6. In this case, the contact force pair is composed of two particles identified by O_A and O_B. Correspondingly, two contact force vectors with the same magnitude but the opposite direction will be obtained instead of the single force vector in the rigid–nonrigid contact algorithm. Once the geometry and physics of the contact are determined, the force integration scheme runs as shown in Fig. 7. Blue and red dashed lines describe the material point rotation configuration. At the same time, the orange and dark green nodes serve for the force transition for two material points, A and B, respectively. It can be found that some nodes are mixed colors, which indicates that multiple materials may possess common nodes. These nodes do not carry a dynamic convection task between different material fields but update their dynamics independently, which is different from the traditional node-based contact algorithms. The traditional one can report unstable numerical results due to the sparse distribution of the common nodes, but the current algorithm eliminates the infect.

3.4. Remarks on the possible error

The rigid–nonrigid and nonrigid–nonrigid contact algorithms adopt the circle material point domain for the contact force integration. The circle shape assumption is based on the isotropic and continuous mechanical response for an infinitesimal element. As long as the number of material points is large enough, the solution domain representing one material point is subtle enough and can be equivalent to a circle without losing too much accuracy. The other reason for the circle shape is that the contact between polygon shapes can be more unstable due to sharp corner. Numerical oscillation may be developed subsequently and leads to errors in simulation results.

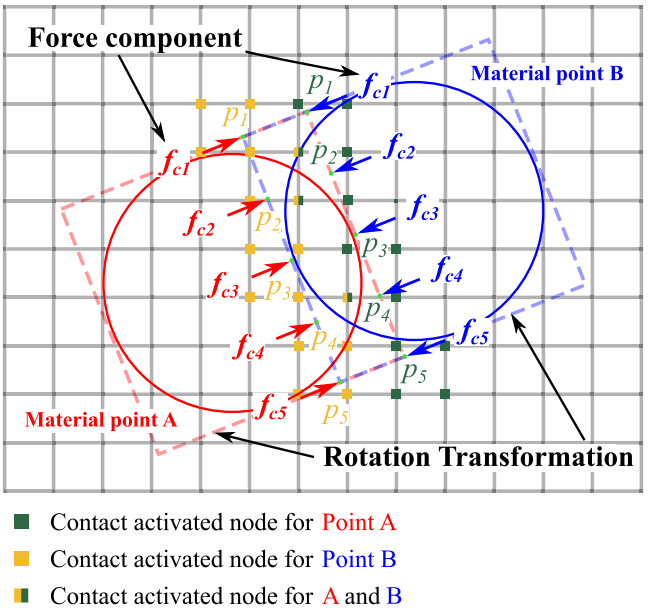

Fig. 7. Nonrigid–nonrigid contact model: Contact force application on the target material point pair. (For interpretation of the references to color in this figure legend, the reader is referred to the web version of this article.)

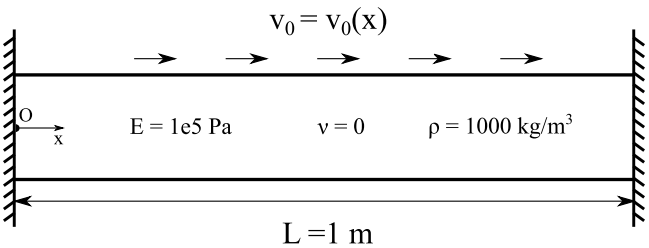

Fig. 8. Schematic diagram of the one-dimensional wave propagation.

4. Verification and validation

4.1. One-dimensional wave propagation

One-dimensional wave propagation has been widely used for the benchmark of numerical implementation [38]. Elastic wave propagation in a two-side fixed bar is used to verify the in-house MPM framework, *SudoMPM*. As shown in Fig. 8, both ends of the bar (Length $L = 1$ m) are constrained in the horizontal direction. An instant velocity field $v_0(x) = x(1 - x)$ is applied on the bar at $t = 0$ s as an initial condition to stimulate an elastic wave. Material properties of the bar are selected as follows: Young's modulus $E = 1 \times 10^5$ Pa, Poisson's ratio $\nu = 0$ and mass density $\rho = 1000$ kg/m^3.

For the specific problem with boundary conditions ($u(0, t) = 0$ and $u(L, t) = 0$, u for displacement) and initial condition ($v(x, 0) = v_0(x)$), analytical solutions are readily obtained as follows:

$$u(x, t) = \sum_{n=1}^{\infty} a_n \sin\left(\frac{n\pi x}{L}\right) \sin(\mu_n t) \tag{19a}$$

$$\mu_n = \frac{n\pi}{L}\sqrt{\frac{E}{\rho}} \tag{19b}$$

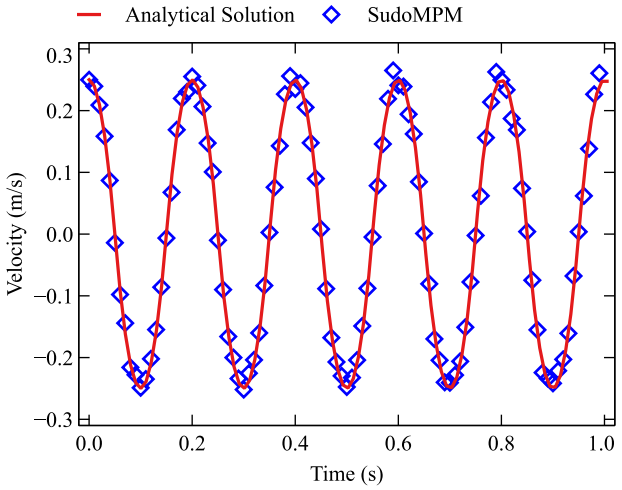

Fig. 9. Evolution of velocity at $L = 0.5$ m obtained from numerical simulation and analytical solution.

$$a_n = \frac{2}{L\mu_n}\int_0^L \sin\left(\frac{n\pi x}{L}\right) v_0(x)dx \tag{19c}$$

$$v(x,t) = \frac{\partial u(x,t)}{\partial t} = \sum_{n=1}^{\infty} a_n\mu_n \sin\left(\frac{n\pi x}{L}\right)\cos(\mu_n t) \tag{19d}$$

Evolution of velocity at the middle of the bar ($L = 0.5$ m) is monitored in Fig. 9. It can be seen that the results obtained from our code (blue diamond) agree well with the analytical solution (red line). Furthermore, the comparison suggests that our MPM framework can accurately reproduce the mechanical response of the one-dimensional wave propagation in elastic materials.

4.2. Interaction between elastic mass and rigid slope: Rotation and translation

4.2.1. Elastic mass toppling on a slope: Rotational dynamics

A rectangle elastic block sitting on a slope can topple once the inclined angle of slope (θ) is greater than a critical value θ_{cr} (the arctangent of the shape aspect ratio of the rectangle). As shown in Fig. 10(a), the dimension of the block is 0.1 m × 0.4 m, and the corresponding θ_{cr} is $\arctan(0.1/0.4) = 14\,^\circ$. The block is assumed perfectly elastic with material properties as follows: density is 3 000 kg/m^3, Young's modulus is 1×10^8 Pa, and Poisson's ratio is 0.22. The cell size of the background grid is 0.02 m, and the block consists of 400 material points. A fixed timestep of 5×10^{-5} s is set for the entire simulation.

A preliminary test with $\theta = 0\,^\circ$ is first carried out to verify the convergence of stress and velocity of the block under rigid–nonrigid contact conditions. The results of the material point at the left-bottom corner of the block are recorded in Fig. 11. It is evident that the stress approaches the analytical solution (self-weight of 1200 N), and the kinematic energy is gradually dissipated to reach an equilibrium state.

Varying inclined angle of the slope will lead to a different dynamic state of the block. Four different slope inclined angles θ (14 °, 16 °, 18 ° and 20 °) are adopted to investigate the rotation evolution of the block. The analytical solution of the toppling can be obtained by integrating the ratio of gravity torque (with respect to the right-bottom corner of the block) and the inertia moment of the block. That is,

$$\alpha_t = 2\arctan\left(\tan\left(\frac{\alpha_0}{2}\right)e^{\frac{GL}{M}t}\right) \tag{20}$$

where α_t and α_0 for current and initial rotation angle; t for current time; G for the gravity of the block; L for the distance between centroid and right-bottom corner of block; M for the inertia moment with respect to the right-bottom corner.

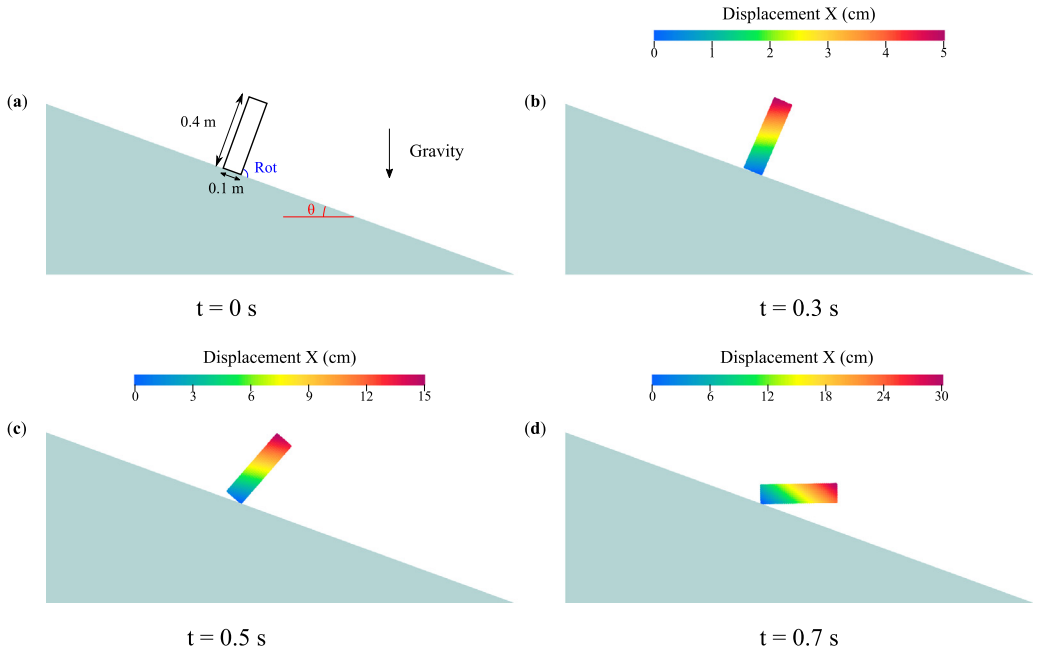

Fig. 10. Toppling of the elastic mass on a slope with inclined angle $\theta = 20\,^{\circ}$, (**a**) schematic diagram for the toppling problem, (**b–d**) for the rotation configuration of the block at time instants of 0.3 s, 0.5 s and 0.7 s.

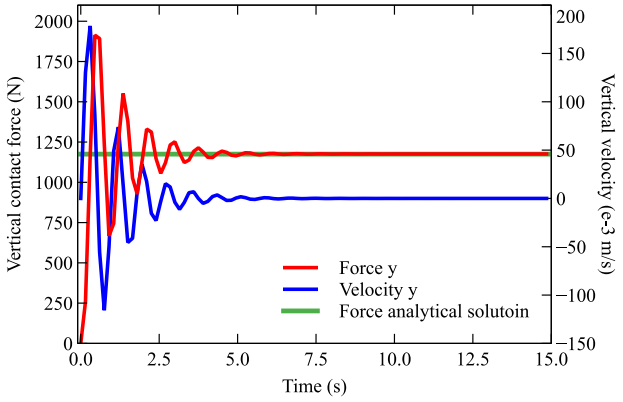

Fig. 11. Convergence of the vertical stress and vertical velocity for the block on a horizontal rigid plane.

Fig. 12 shows the evolution of the rotation angle of the block (marker) and the analytical solutions (line) for four different inclined angles θ. With the decrease of θ, the tendency of the toppling weakens and disappears at around the critical value $\theta_{cr} = 14\,^{\circ}$. Moreover, the contour of the horizontal component of the displacement field for the toppling block at $\theta = 20\,^{\circ}$ is represented in Fig. 10(b–d). These results demonstrate that the rigid–nonrigid contact algorithm can capture contact rotation dynamics with reasonable accuracy.

4.2.2. Elastic mass sliding along a slope: Translational dynamics

An elastic mass sliding along a slope is simulated to further verify the translational dynamics for rigid–nonrigid contact algorithm. As shown in Fig. 13, a 2 m $\times$ 2 m block mass (blue) is positioned on a frictional slope with an inclined angle of $\theta = 45\,^{\circ}$ and a friction coefficient of $\mu = 0.5$. The block mass is discretized into 16 $\times$ 16 cells with a single material point per cell. Elastic material properties with Young's modulus ($E = 1 \times 10^7$ Pa) and

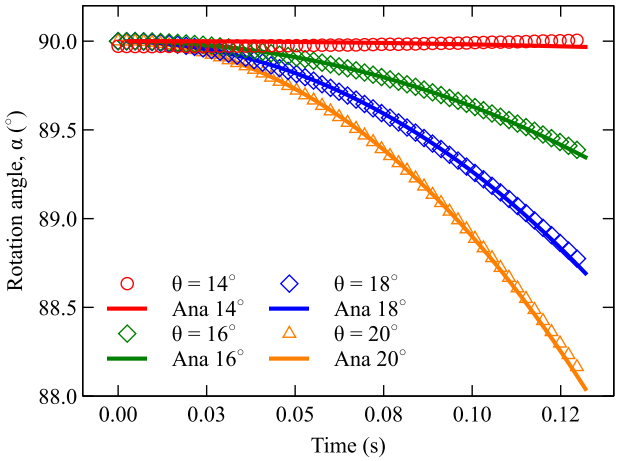

Fig. 12. The rotation angle of the block as a function of time for varying inclined angles of slope.

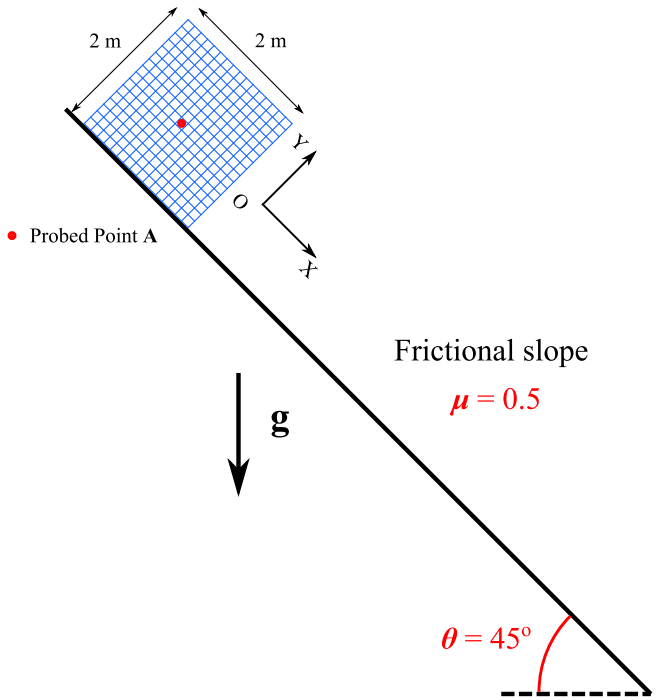

Fig. 13. Setup of a block sliding along a slope under gravity. (For interpretation of the references to color in this figure legend, the reader is referred to the web version of this article.)

Poisson's ratio ($\nu = 0.2$) are assigned to these material points. The block then slides along the slope, driven by gravity. The simulation lasts for $t = 2$ s with a fixed timestep of 0.0001 s.

Existing studies have reported that the traditional contact algorithms pursue the accuracy of the bidirectional mapping between material points and background nodes. For example, Hammerquist and Nairn [39] makes the contact detection criteria strict by adding additional displacement criteria to the existed approaching velocity criteria to eliminate the early contact ill condition. As a result, contact can occur if and only if two material is approaching each other, plus their relative displacement is less than a given threshold. The velocity contact criteria strengthened with the relative displacement detection allows more kinematics (both displacement and velocity) to be mapped from material points to nodes and is expected to achieve an exact contact solution.

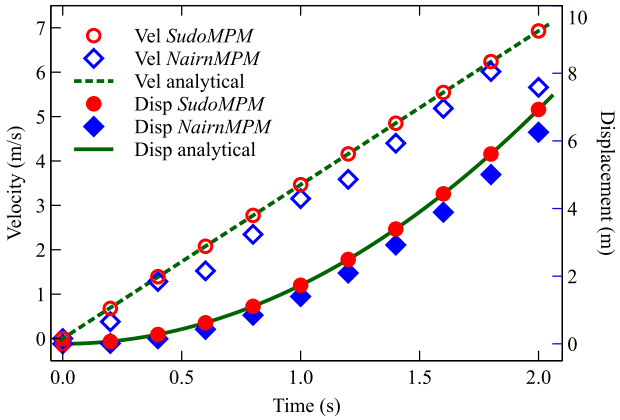

Fig. 14. Mechanical response of probed point A under contact algorithm of *NairnMPM* (blue) and *SudoMPM* (red). (For interpretation of the references to color in this figure legend, the reader is referred to the web version of this article.)

The mechanical response of the probed Point A (center of the mass) is selected to quantitatively compare the contact algorithm of Hammerquist and Nairn [39] and our code, *SudoMPM*. As shown in Fig. 14, red and blue markers depict the evolution of velocity and displacement for Hammerquist and Nairn [39] and *SudoMPM*, respectively. Meanwhile, dashed and solid green lines demonstrate the corresponding analytical solutions. It can be seen that the velocity from Hammerquist and Nairn [39] fluctuates slightly around the analytical one. Moreover, both velocity and displacement obtained from Hammerquist and Nairn [39] exhibit an over-damping manner. By contrast, *SudoMPM* predicts precise trends for both velocity and displacement. The difference between these two contact algorithms may imply that though complicated contact models have been integrated into the traditional contact algorithm to resolve the material contact gradually, the algorithm improvement can still be confined by the inherent drawbacks of MPM. Other advanced algorithms like the two-mapping scheme of [20] and XPIC scheme of [21] enhance the accuracy and stability of the contact algorithm significantly; however, they are accompanied by larger computation overhead. In this sense, our proposed discrete-element-based contact algorithm can be a promising alternative to those complicated algorithms dealing with node dynamics.

4.3. Interaction between a rigid pile and soils: Quasi-static problems

Multi-material contact problems involving the rigid boundary condition, e.g., the soil–structure interaction in geotechnical engineering, demand a higher requirement for the robustness of the contact algorithm [40]. As noted in Section 3, numerical instabilities can be encountered during the contact state solution process, assisted by the nodal dynamics. Particularly, if the rigid intruder serves as a complex shape boundary, the existed contact algorithm may face greater numerical instability even reinforced by the MP-DEM solution strategy [24]. As a widespread geotechnical problem, pile installation involves soil–structure interaction in conjunction with large deformation. In this respect, pile installation can be a suitable benchmark for contact algorithms. The literature has reported the unique role MPM plays in handling the significant deformation and the challenge MPM meets in defining the soil–structure interface. Given that, a pile penetration case is used here to introduce our contact algorithm to the soil–structure problem and strives to illustrate the effectiveness of the rigid–nonrigid contact solver on practical problems.

A schematic diagram of the pile installation model under plane strain conditions is shown in Fig. 15. The pile is considered as a rigid material with a scaled standard cone tip ($R = 0.4$ m, $\theta = 30°$), length ($L = 6$ m) and a pre-defined penetration depth ($L_p = 9R = 3.6$ m). The simulation domain of the soil is set as width $W = 8$ m and height $H = 4.8$ m. The bottom boundary of the soil is fixed in both horizontal and vertical directions, while the right boundary only has the horizontal displacement fixed. Note that the left boundary does not serve as a boundary condition but is intended to mimic a half model instead. Resolution of material point distribution, i.e., material points within each element, is one for the entire domain, and 4 900 material points are generated in this simulation.

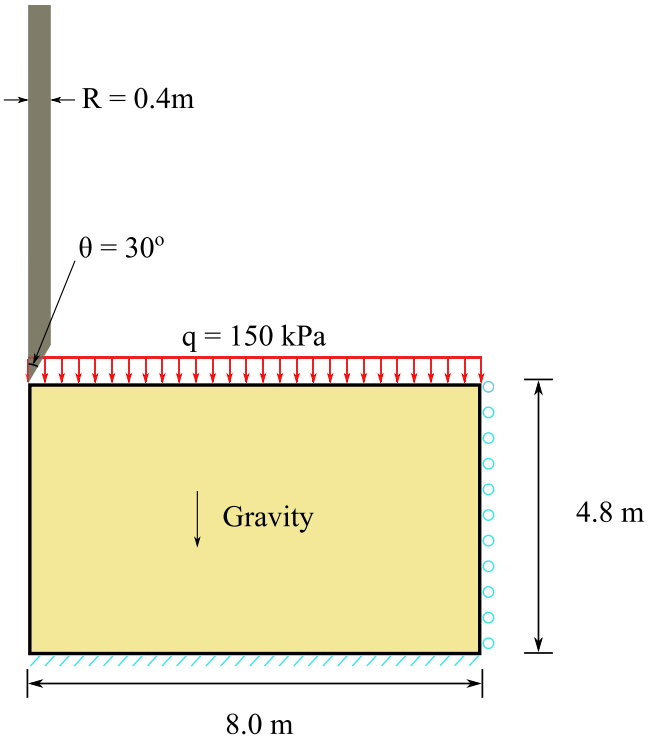

Fig. 15. Initial configuration of the pile installation.

Mohr–Coulomb model is taken as the constitutive material model of the soil, where material properties are selected from Susila and Hryciw [41] as: mass density ($\rho = 1620$ kg/m^3), Young's modulus ($E = 1.6 \times 10^7$ Pa), Poisson's ratio ($\nu = 0.3$), cohesion ($c = 0$ kPa), friction angle ($\phi = 32\,^\circ$), dilation angle ($\psi = 0.01\,^\circ$) and Rankine's tension cut-off ($t_c = 0.01$ kPa). Gravity loading along with the artificial particle damping ($D_p = 1.0$) and PIC fraction (PIC = 1.0) is performed prior to the penetration. Once the geo-static stress remains stable, a surcharge of 150 kPa is applied to the upper surface of the soil. Then, the pile is driven downwards by a constant velocity ($v_p = -0.1$ m/s), and particle damping and PIC fraction are set to 0.7 for a quasi-static penetration process.

Fig. 16 presents the profile of the cone stress versus the normalized penetration depth of both Susila and Hryciw [41] and this study. The cone stress is defined as, $q_c = f_c/R$, where f_c for reaction of force of cone tip and $R = 0.4$ m for radius of cone tip. The red line depicts the result from the novel contact algorithm. It can be observed that the q_c of Susila and Hryciw [41], where the Arbitrary Lagrangian–Eulerian technique is utilized, reaches a stable value with about 5 MPa. The result of this study gives a similar trend and critical value of q_c as that in Susila and Hryciw [41]. The difference between these results is that the fluctuation appears for this algorithm when $z/R \geqslant 3$. The reason may be attributed to the iteration scheme during the solution process. FEM adopts the implicit iteration for the penetration while our MPM takes an explicit iteration. The dynamic response terms in MPM cannot vanish even though relatively high damping is enforced. The small disturbance induced by the dynamic wave propagation results in the divergence of these two results.

The contours of stress component magnitudes (XX, YY and XY) are shown in Fig. 17. It can be seen that the stress level around the cone tip is much more significant than the region around the shaft, and the vertical stress magnitude around the section of the penetrator increases as the coordinate Y decreases. However, the horizontal stress magnitude displays a complex distribution along the axis Y. A small neighboring region above the cone tip can hold a lower stress level than the upper shaft region, and this phenomenon is also reported by Susila and Hryciw [41]. The reason may be that the shape characteristic of the cone tip leads to a stress magnitude transition within the joint region between the tip and the shaft. The shape switching from the rectangle (shaft) to the cone (tip) causes the discontinuity of the frictional force field, thereby triggering the stress redistribution and leading to the final dip around the interface between the shaft and tip.

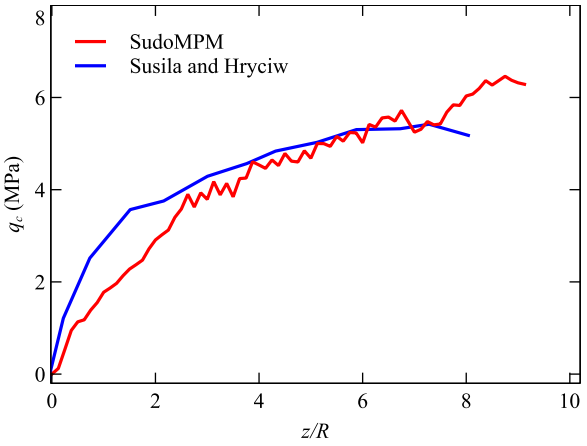

Fig. 16. Cone tip resistance versus the normalized penetration depth.

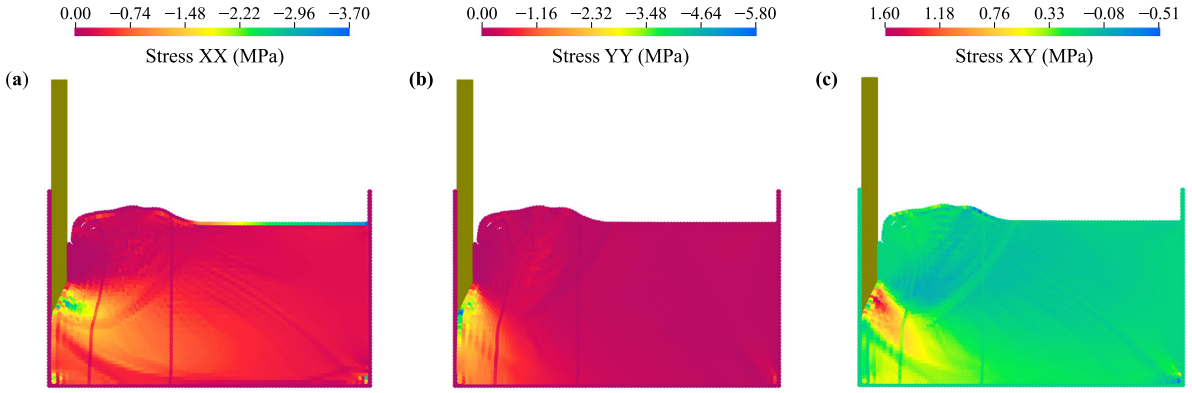

Fig. 17. Stress distribution at the critical state for components **(a)** stress XX, **(b)** stress YY and **(c)** stress XY.

The displacement fields at the critical state of the penetration are shown in Fig. 18, where the sub-figures (a) and (b) present the displacement contour and vector in the horizontal and vertical direction, respectively, and sub-figure (c) demonstrates the equivalent shear strain. Figs. 18(a and b) offer an intuitive representation of the soil response against the cone penetration, as the soil is pushed away from the cone penetrator and forms smooth displacement distributions close to the shaft and the cone tip. Meanwhile, those material points attaching to the shaft move downward, driven by the frictional force. Material points that are undertaken the surcharge in the top surface layer behave in a complex mode combining the shrink towards the shaft and the upturning toward the top direction. As a result, they suffer from high deformation and rotation. The dramatic distortion of the material point integration domain in the penetration process is an intractable issue, which can influence the numerical results for the mesh-free algorithm strengthened by the conventional contact algorithm. The unstable contact solution of MPM results from the wrong DOF settings of nodes. Moreover, it may contribute to the incapability of the free surface simulation during the large deformation penetration. In detail, the node-wise contact algorithms always approximate the cone penetrator by clusters of rigid material points imposed by horizontal and vertical constraints. The kinematic mapping from rigid material points to the nodes does not transit physical state variables like momentum and mass. However, it does lock all the node DOFs in both compress and tension directions. Consequently, the material points within the free surface will not be pushed away as expected. Furthermore, a reasonable boundary condition imposition cannot

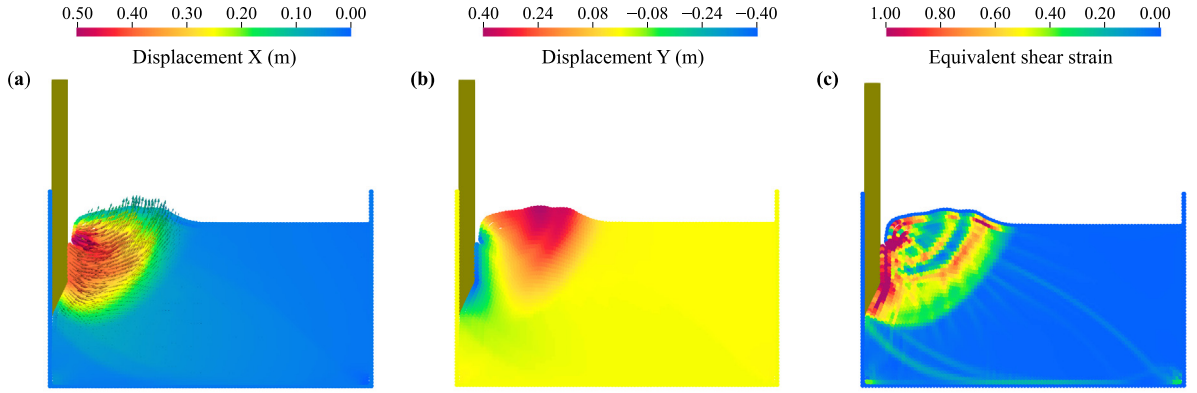

Fig. 18. Displacement contour at the critical state for components **(a)** horizontal displacement, **(b)** vertical displacement and **(c)** equivalent shear strain.

be guaranteed under the condition of a conventional contact algorithm. However, our proposed contact algorithm can make a difference from the perspective of the direct interaction between material points and convex rigid shapes.

4.4. Interaction between non-rigid bodies

4.4.1. Interaction between two elastic rings

The ring collision example is used to test our non-rigid material contact algorithm. The literature has mentioned the tensile instability faced in the simulation of the collision of two approaching cylinders [42]. The development of fragmentation of the rings characterizes the tension instability during the collision process, and the robustness of the contact algorithm can be evaluated as well.

Two identical elastic rings approach to collide under the 2D plane strain condition, as shown in Fig. 19(a). The outer and inner radii are set as $r_{out} = 40$ mm and $r_{in} = 30$ mm, respectively. Initial velocities of $v_0 = 30$ m/s and -30 m/s are assigned to the left and right rings, respectively. A uniform background grid is setup with a cell size of 1.6 mm and 4 material points per cell. As a consequence, 6 890 material points were generated in total. Material for rings is assumed to be NeoHookean material: Young's modulus $E = 7.3 \times 10^7$ Pa and Poisson's ratio $\nu = 0.4$. Non-rigid contact properties are as follows: normal stiffness $K_n = 1 \times 10^7$ N/m^2, tangential stiffness $K_s = 1 \times 10^7$ N/m^2 and friction coefficient between two rings $\mu = 0.2$. Note that no damping is imposed in this example. The simulation runs 3.8 ms with a fixed timestep of 1×10^{-6} s.

Fig. 19 illustrates the snapshots of displacement contour during the course of collision. The two rings touch each other at $t = 0.2$ ms (Fig. 19(b)), and then their mechanical responses induced by the impact and rebound are driven by the non-rigid DEM-wise contact algorithm. The gray contour lines that are plotted on the same snapshot depict the motion of rings from Huang et al. [20]. It suggests that our contact scheme can reproduce the ring collision as well as the mesh-wise material point contact algorithm [20]. For a comprehensive validation of this contact algorithm, the variation of the energy components is recorded in the simulation process. The evolution of the energy components such as kinetic energy ($E_k = \sum_p \frac{1}{2} m_p v_p^2$), strain energy ($E_s = \sum_p \frac{1}{2} \sigma_{p,ij} \epsilon_{p,ij} V_p$) and total energy ($E_{tol} = E_k + E_s$) of this study and Huang et al. [20] are plotted in Fig. 20, where the energy components and the elapsed time are normalized by the total energy and the total simulation time, respectively. Blue and red lines show the variation of E_k and E_s against the time, respectively, while green and brown lines provide the comparison between the total energy from this study and that of Huang et al. [20]. Results demonstrate a high agreement between the total energy from this study and Huang et al. [20], which indicates the robustness of the energy reserve of this nonrigid–nonrigid contact algorithm. Apart from the kinematic and strain energy component, contact potential is listed here. This component counts the energy saved at the particle penetration depth and is a unique component when the DEM contact engine is considered. As can be seen, the contact potential increases immediately after

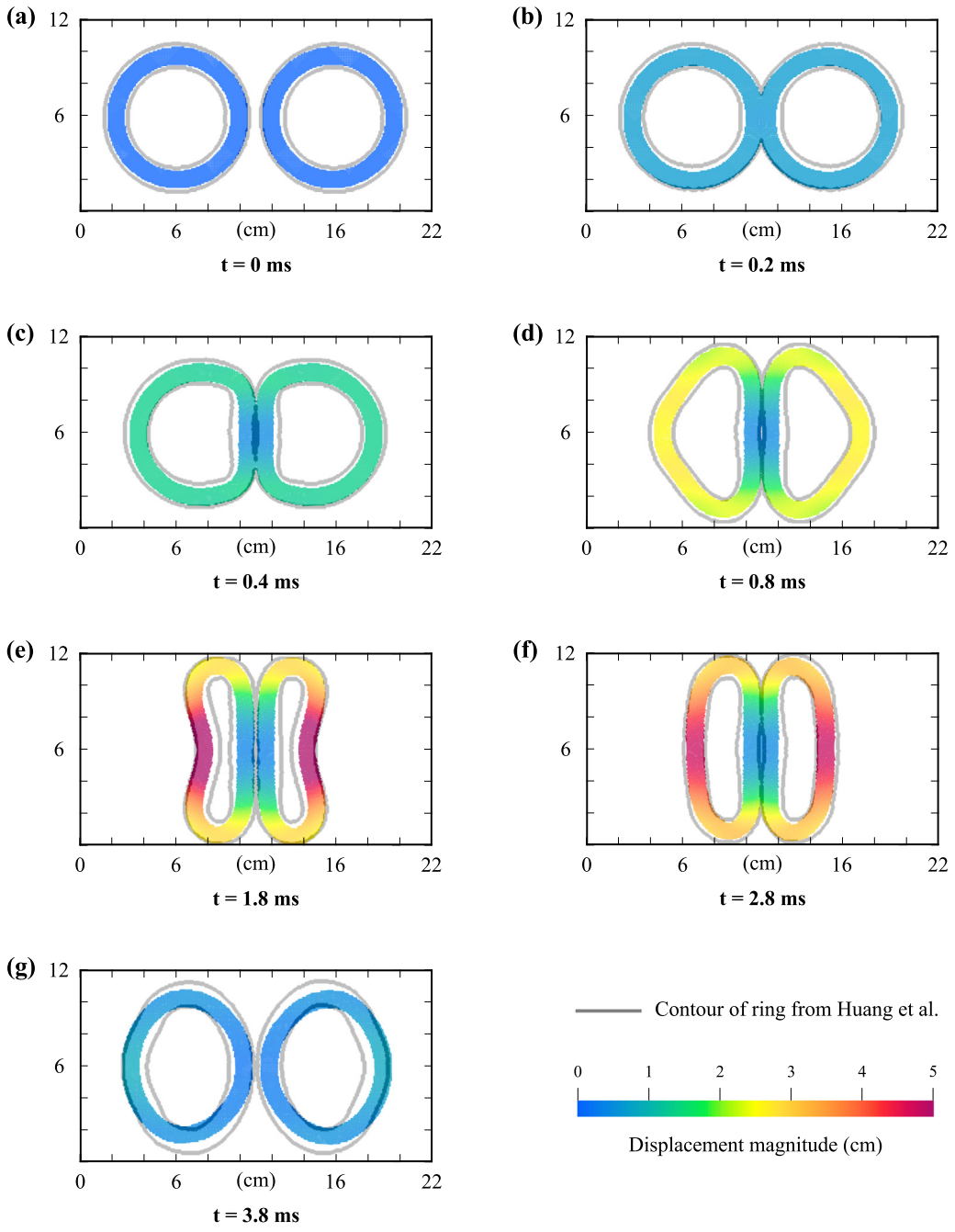

Fig. 19. Head-on impact of two identical elastic rings: simulation snapshots (**a**-**g**). The units are mm for length and ms for time. (For interpretation of the references to color in this figure legend, the reader is referred to the web version of this article.)

two rings kiss each other, then decreases with the separation of the rings going. The new contact algorithm can be a trade-off between accuracy and efficiency. The contact normal and contact detection can be intuitive as the DEM code, reflecting the particle scale behavior and reserving the energy. Furthermore, our contact algorithm is less reliant on the nodal resolution than the conventional and be with good flexible and extensible. More than two

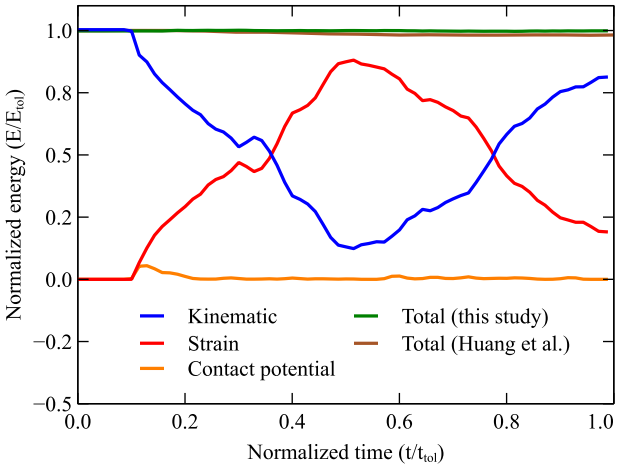

Fig. 20. Evolution of kinetic energy, strain energy, contact potential energy and the total energy for the collision of two elastic rings. (For interpretation of the references to color in this figure legend, the reader is referred to the web version of this article.)

materials can be handled simultaneously in the contact framework, which allows a complex multi-material contact condition.

4.4.2. Interaction between two elastic disks

The previous example demonstrates the energy and tension stability of the nonrigid–nonrigid contact algorithm. Furthermore, one of the Hertz contact problems, two cylinders collision, is selected here to benchmark the nonrigid–nonrigid contact algorithm. Under the plane strain condition (2D), the two-cylinder contact algorithm is simplified to a two-disk contact problem. Given two elastic disks with radius of R_1 and R_2, Young's modulus of E_1 and E_2, and Poisson's ratios of ν_1 and ν_2, respectively, as shown in Fig. 21(a), the analytical relationship between the contact force (F) and contact region (a) can be given as [43],

$$F = \frac{\pi E^* L a^2}{4R^*} \tag{21a}$$

$$\frac{1}{E^*} = \frac{1-\nu_1^2}{E_1} + \frac{1-\nu_2^2}{E_2} \tag{21b}$$

$$\frac{1}{R^*} = \frac{1}{R_1} + \frac{1}{R_2} \tag{21c}$$

where E^* and R^* are the equivalent Young's modulus and radius, respectively; L is the length of the cylinder and is set to 1 for plane strain condition; a is the contact region and is given by $a = \sqrt{R^* d}$, where d is the indentation depth.

In the simulation, the two disks hold the same radius (0.01 m) and material properties according to Guilkey et al. [27] as follows: Young's modulus is 9.4×10^{10} Pa, and Poisson's ratio is 0.07. The combination of two different grid cell sizes (size = $R/20$, $R/40$) and two particles per cell (PPC = 1, 4) contributes to four different material point resolutions (material point numbers of 2 528, 10 048, 10 048 and 40 216). An additional two-disk collision with the rotation configuration of 45 ° compared to the grid is investigated to doublecheck the robustness of the algorithm on local rotation coordinate. The collision occurs by forcing opposite ramping-up body forces on the two disks. The simulation runs 0.2 s with a fixed timestep of 1×10^{-6} s.

The displacement magnitude fields at the initial, middle and final stage of the contact problem are shown in Fig. 21(b–d), and the relationship between the contact force and the contact region is plotted in Fig. 22. Although a slight difference between the numerical and analytical results is observed, the nonrigid–nonrigid contact algorithm can capture the collision dynamics of two disks well. Moreover, with the resolution increases, the curve of the numerical result approaches the analytical one but with negligible small deviation, suggesting that the proposed contact algorithm shows a negligible dependence on the grid resolution.

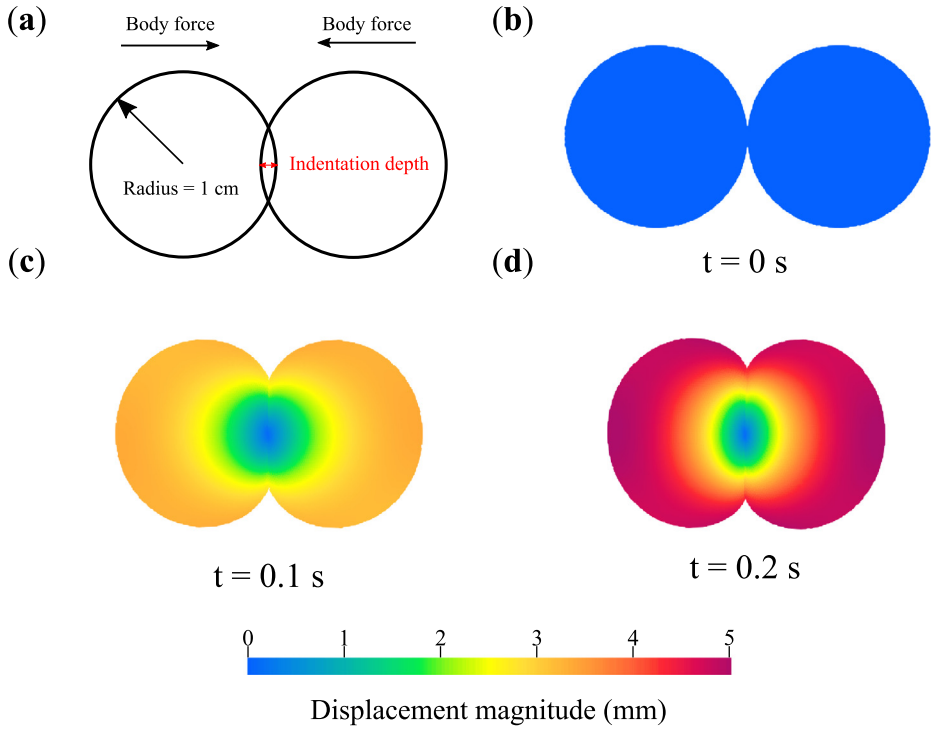

Fig. 21. Collision between two elastic disks: The schematic diagram (**a**) and displacement contours at different time instants of (**b**) 0 s, (**c**) 0.1 s and (**d**) 0.2 s.

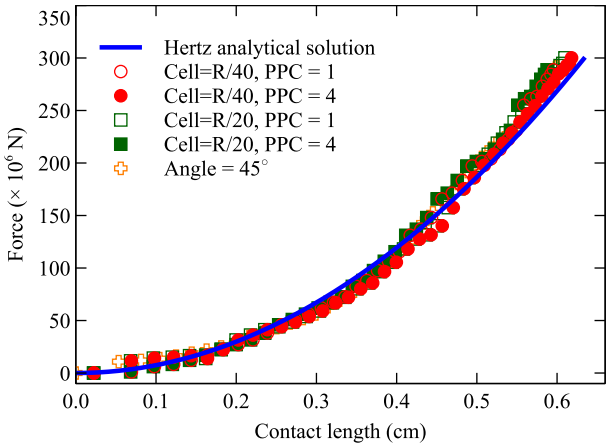

Fig. 22. The variation of the contact force against the contact region for different material point resolutions and rotated boundary condition.

4.5. Dynamic impact problems: Granular collapse and dam break

Granular collapse [44] and granular flow impact problems demand contact algorithm with high numerical stability [45,46]. This section introduces two typical dynamic impact problems (granular collapse and dam break) to further validate the algorithms of rigid–nonrigid and nonrigid–nonrigid interaction.

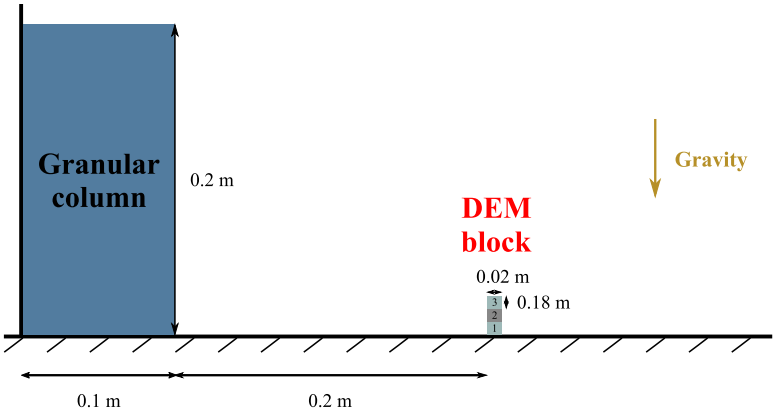

Fig. 23. Simulation setup of granular collapse with impact on stacked rigid blocks.

4.5.1. Granular collapse: Interaction between granular column and rigid block

The simulation setup is illustrated in Fig. 23, following the experimental test by Liu et al. [24]. The granular column collapses and impact the three stacked wooden blocks under gravity, where Block 1 is fixed on the ground and the other two blocks will move due to impact. The material constitutive model is the Drucker–Prager model with the same parameter values as in Liu et al. [24] where an MPM-shrunken DEM framework was benchmarked against the experimental test. A total of 8 192 material points are generated, and the timestep is set as 1×10^{-4} s.

Fig. 24 reports a comparison between the experimental and numerical results. The granules reach the rigid block at about $t = 0.25$ s, and the top two blocks suffer from dramatic dynamics evolution. The interaction lasts for about 0.15 s, and Block 2 ends up resting on the ground at about $t = 0.4$ s. The detailed rotation of Block 2 is monitored in Fig. 25 for quantitative comparison. It can be observed that our contact algorithm can well capture the evolution of the rotation of Block 2 and the angle difference is around 5 °. In the final stage, our results indicate that the space between Blocks 1 and 2 is occupied by the material points as observed in the experimental results, which reflects the natural energy exchange between the granules and the rigid block. Overall, our numerical results are consistent well with the experimental one in terms of either the free surface line or the energy transfer, suggesting that our generalized contact algorithm is numerically stable for impact problems.

4.5.2. Dam break: Interaction between fluid and cantilever beam

Similar to the granular collapse simulation in the previous subsection, the stacked rigid blocks are replaced by an elastic cantilever beam, and the Newtonian liquid (water) takes over the granular column to simulate dam break so as to validate the nonrigid–nonrigid contact algorithm. The simulation setup follows an experimental test in Liao et al. [47]. A 0.2 m × 0.4 m water column (cyan) is set up together with a cantilever beam (gray) of 0.004 m (width) × 0.1 m (height), as shown in Fig. 26. Three probed points (A, B and C) are selected for the horizontal displacement comparison between the experimental and numerical results. A uniform background grid with a cell size of 0.002 m is employed, where each cell initially consists of 1 material point for water and 4 material points for beam. Thus, there are $100 \times 200 \times 1 = 20\,000$ material points for water, and $2 \times 50 \times 4 = 400$ material points for the solid beam.

The beam is assumed as linear elastic and all the material properties are same as that of Liao et al. [47] with Young's modulus $E_S = 3.5 \times 10^6$ Pa and Poisson's ratio $\nu_S = 0.45$. Its mass density is $\rho_S = 1161.54$ kg/m^3. As for water, the relationship between stress and strain under the Stokes condition ($\lambda = \frac{2\mu}{3}$) is:

$$\boldsymbol{\sigma} = 2\mu_w \dot{\boldsymbol{\epsilon}}' - p\mathbf{I} \tag{22a}$$

$$p = K\left[\left(\frac{\rho}{\rho_0}\right)^{\gamma} - 1\right] \tag{22b}$$

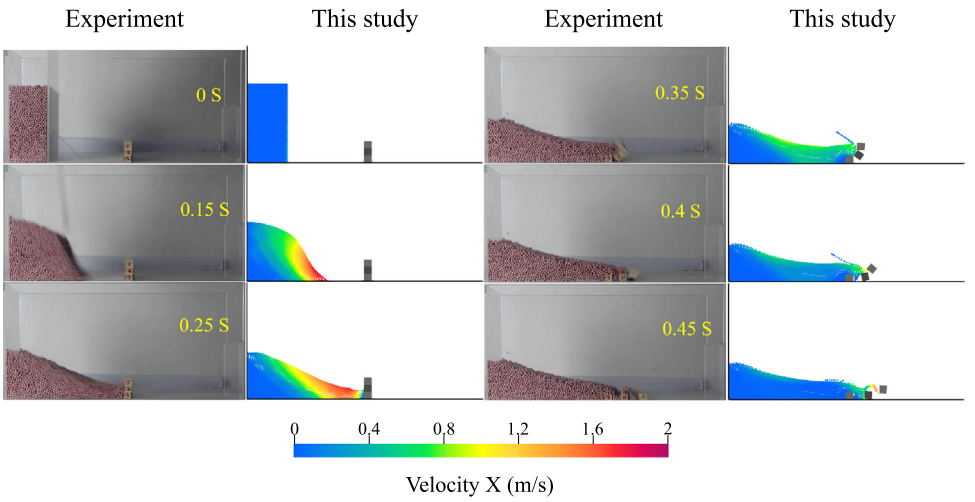

Fig. 24. Snapshots of a granular column impacting wooden blocks at different time instants. Note that the experimental results are from Liu et al. [24].

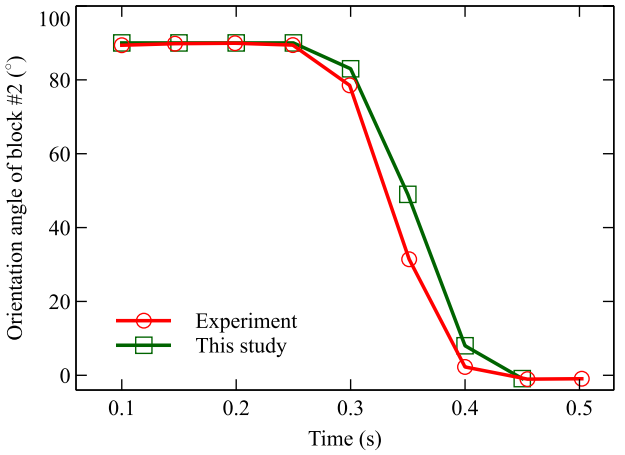

Fig. 25. The evolution of the rotation angle of Block 2 from experimental [24] and our numerical results.

where $\mu_w = 8.9 \times 10^{-4}$ Pa·s is the dynamic viscosity for water; $\dot{\boldsymbol{\epsilon}}'$ is the deviatoric incremental strain, and p is the pressure obtained from the equation of state (EOS). Eq. (22b) gives the detail of the EOS introduced by Monaghan [48] and Cueto-Felgueroso et al. [49], where K for bulk modulus of water ($K = 3 \times 10^4$ Pa), ρ for current mass density and ρ_0 for initial mass density ($\rho_0 = 997$ kg/m^3). Coefficient γ is a state variable and set to 7 for water. Note that the normal contact stiffness between the liquid and solid is $K_n = 3 \times 10^6$ N/m^2 and shear contact stiffness is $K_s = 1.5 \times 10^6$ N/m^2, and the friction coefficient between liquid and solid is $\mu = 0.2$.

A geostatic procedure is carried out before the simulation started via the constraint provided by the two fixed walls (the right wall is omitted in the schematic diagram). Damping coefficients (particle damping 1.0 and grid damping 1.0) combined with the PIC fraction of 1.0 are introduced in this stage for a quick particle kinematics dissipation. Once the stress fluctuation is less than a specific threshold, the dam break is triggered by removing the right wall. Meanwhile, the PIC fraction is changed to 0.001, intending to eliminate artificial energy dissipation. The total simulation time is 1 s, and the timestep is 5×10^{-5} s.

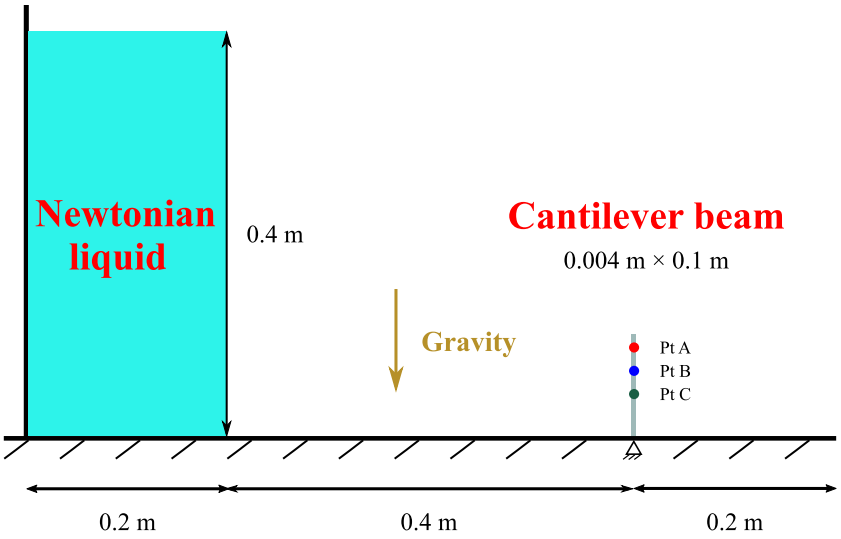

Fig. 26. Simulation setup of dam break with impact on a cantilever beam. (For interpretation of the references to color in this figure legend, the reader is referred to the web version of this article.)

Fig. 27 shows the simulation snapshots under the nonrigid–nonrigid contact algorithm. The first stage of the impact starts at around $t = 0.25$ s, and the collision lasts about 0.05 s. Then the liquid rebounds from the boundary at $t = 0.55$ s and interacts with the beam from the back side between 0.55 s and 0.8 s. The comparison of the displacement of the three probed points is given in Fig. 28, which shows that our contact algorithm can capture most of the characteristics of the fluid–solid interaction. The numerical results collapse well with experimental one from $t = 0.25$ s to $t = 0.4$ s and the result also demonstrate a similar decreasing tendency of displacement for three probed points from the $t = 0.4$ s to $t = 0.8$ s. The difference centers around the decreasing tendency from $t = 0.8$ s to the end. The experimental result indicates a strong decreasing tendency of horizontal displacement for all three points, while our results give a moderate decrease. A possible reason is associated to the numerical method of fluid dynamics handling. Our MPM simulates the behavior of the fluid using a straightforward way in terms of the stress–strain relationship, which may be incapable of considering the turbulence and air cavity coming from the first and second impact, thereby leading to a propagation of the numerical oscillation. Coincidentally, that is why the experimental results demonstrate a more obvious deformed profile of the beam than this study at the beginning of the impact. Moreover, other factors such as air–fluid mixture and dynamics iteration scheme may affect the numerical results, which is, however, beyond the scope of this study. Overall, the proposed nonrigid–nonrigid algorithm can effectively reproduce the dynamics of the fluid–structure interaction.

Remarks. The multi-material interaction associated with gravity-driven rigid–nonrigid and nonrigid–nonrigid cases show that the proposed nonrigid–nonrigid contact algorithm can be a robust alternative to the traditional MPM contact algorithm.

5. Summary

A generalized contact scheme has been proposed within a MP-DEM contact framework for multi-body, multi-material interaction problems, where a DEM-enhanced inter-particle contact model is introduced to bypass the node-wise contact detection criteria. Such a generalized and hybrid contact scheme helps to effectively mitigate the early contact ill condition commonly encountered in traditional node-based contact algorithms of MPM. Moreover, the proposed contact scheme is flexible to be extended for advanced contact models and even multi-body interaction with complex shapes.

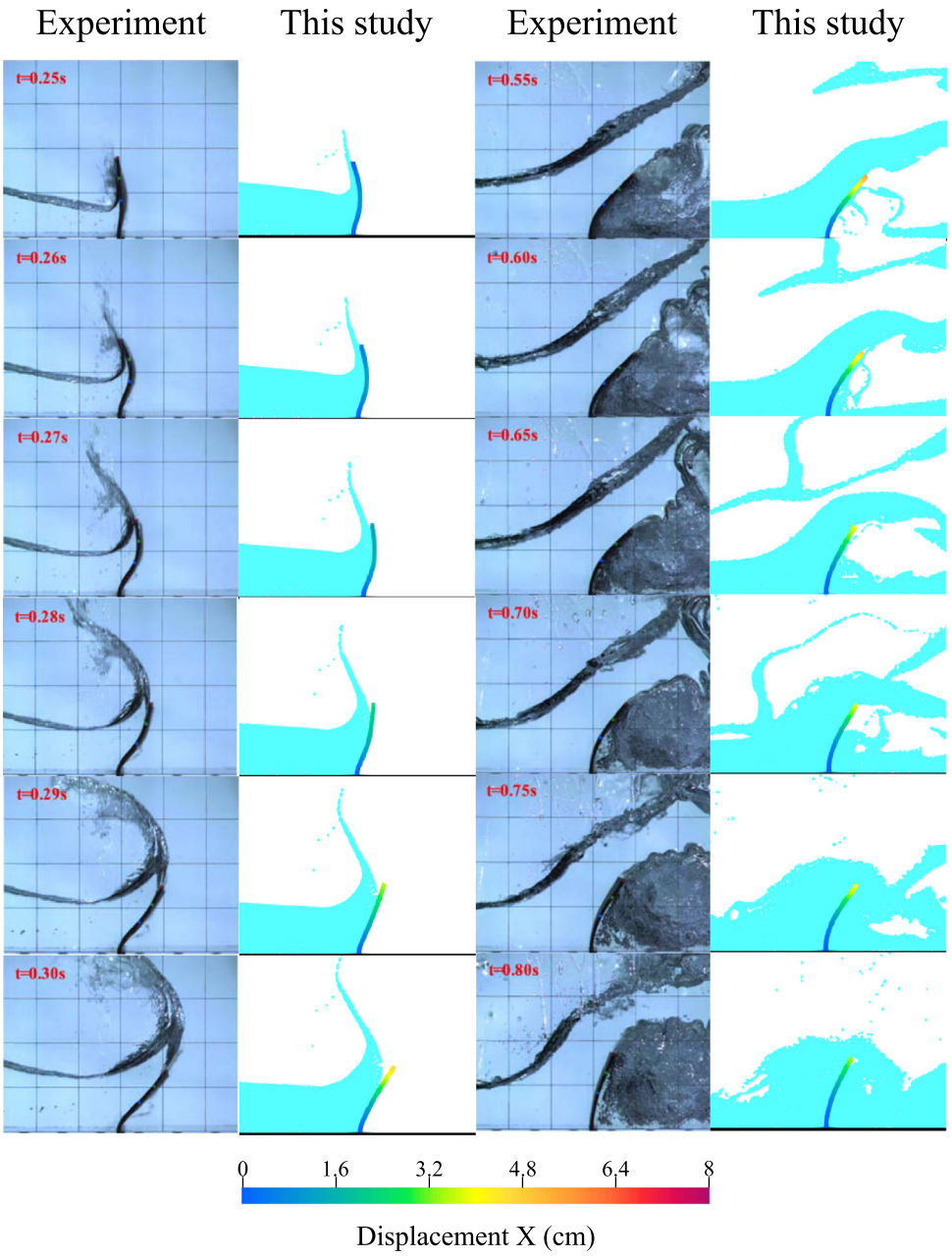

Fig. 27. Horizontal displacement contours of the cantilever beam due to the impact from liquid at different time instants. Note that the experimental results are from Liao et al. [47].

A series of numerical cases have been employed to verify and benchmark the new contact scheme, including 1D wave propagation, toppling and sliding problems for rotational and translational dynamics, pile installation, rings and disks collision, and dynamic impacts in granular collapse and dam break. The numerical results agree well with the analytical results or that from the experiments. Our proposed contact scheme remains numerical stable for such challenging contact problems where dynamics exchange occurs among multi-materials, which may pave an effective way for large-deformation simulations involving multi-body and multi-material problems using MPM.

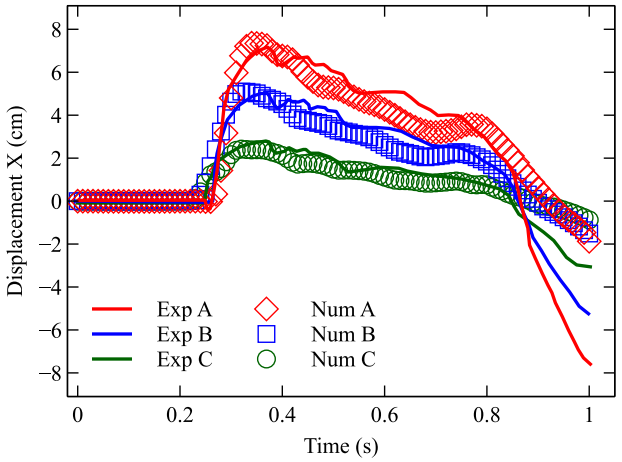

Fig. 28. Comparison of horizontal displacement of probed points (A, B and C) between the experimental from Liao et al. [47] and our numerical results.

Declaration of competing interest

The authors declare that they have no known competing financial interests or personal relationships that could have appeared to influence the work reported in this paper.

Data availability

No data was used for the research described in the article.

Acknowledgments

This work was financially supported by the National Natural Science Foundation of China (by Project No. 51909095 and No. 11972030), the Guangdong Basic and Applied Basic Research Foundation (2022A1515010848), Research Grants Council of Hong Kong (by GRF Project No. 16211221 and No. 16206322), and the Project of Hetao Shenzhen-Hong Kong Science and Technology Innovation Cooperation Zone (HZQB-KCZYB-2020083). Any opinions, findings, and conclusions or recommendations expressed in this material are those of the authors and do not necessarily reflect the views of the financial bodies.

References

[1] D. Sulsky, Z. Chen, H.L. Schreyer, A particle method for history-dependent materials, Comput. Methods Appl. Mech. Engrg. 118 (1–2) (1994) 179–196.
[2] D. Sulsky, S.-J. Zhou, H.L. Schreyer, Application of a particle-in-cell method to solid mechanics, Comput. Phys. Comm. 87 (1–2) (1995) 236–252.
[3] D.J. Benson, An efficient, accurate, simple ALE method for nonlinear finite element programs, Comput. Methods Appl. Mech. Engrg. 72 (3) (1989) 305–350.
[4] Y. Hu, M. Randolph, A practical numerical approach for large deformation problems in soil, Int. J. Numer. Anal. Methods Geomech. 22 (5) (1998) 327–350.
[5] D. Wang, Y. Hu, M.F. Randolph, Three-dimensional large deformation finite-element analysis of plate anchors in uniform clay, J. Geotech. Geoenviron. Eng. 136 (2) (2010) 355–365.
[6] H. Sabetamal, J.P. Carter, X. Zhang, D. Sheng, Coupled analysis of full flow penetration problems in soft sensitive clays, Comput. Geotech. 133 (2021) 104054.
[7] J.S. Kwan, E.H. Sze, C. Lam, Finite element analysis for rockfall and debris flow mitigation works, Can. Geotech. J. 56 (9) (2019) 1225–1250.
[8] C.W.W. Ng, Y. Su, C.E. Choi, D. Song, C. Lam, J. Kwan, R. Chen, H. Liu, Comparison of cushioning mechanisms between cellular glass and gabions subjected to successive boulder impacts, J. Geotech. Geoenviron. Eng. 144 (9) (2018) 04018058.
[9] R. Zhang, Y. Sun, E. Song, Simulation of dynamic compaction and analysis of its efficiency with the material point method, Comput. Geotech. 116 (2019) 103218.

[10] W. Sołowski, S. Sloan, Evaluation of material point method for use in geotechnics, Int. J. Numer. Anal. Methods Geomech. 39 (7) (2015) 685–701.
[11] A. Tombari, M.H. El Naggar, F. Dezi, Impact of ground motion duration and soil non-linearity on the seismic performance of single piles, Soil Dyn. Earthq. Eng. 100 (2017) 72–87.
[12] K. Soga, E. Alonso, A. Yerro, K. Kumar, S. Bandara, Trends in large-deformation analysis of landslide mass movements with particular emphasis on the material point method, Géotechnique 66 (3) (2016) 248–273.
[13] M. He, L.R. e Sousa, A. Müller, E. Vargas Jr., R. Sousa, C.S. Oliveira, W. Gong, Numerical and safety considerations about the Daguangbao landslide induced by the 2008 Wenchuan earthquake, J. Rock Mech. Geotech. Eng. 11 (5) (2019) 1019–1035.
[14] Y. Dong, D. Wang, M. Randolph, Quantification of impact forces on fixed mudmats from submarine landslides using the material point method, Appl. Ocean Res. 102 (2020) 102227.
[15] C.W.W. Ng, C.E. Choi, A. Su, J.S. Kwan, C. Lam, Large-scale successive boulder impacts on a rigid barrier shielded by gabions, Can. Geotech. J. 53 (10) (2016) 1688–1699.
[16] R. Ma, W. Sun, A finite micro-rotation material point method for micropolar solid and fluid dynamics with three-dimensional evolving contacts and free surfaces, Comput. Methods Appl. Mech. Engrg. 391 (2022) 114540.
[17] S.G. Bardenhagen, E.M. Kober, The generalized interpolation material point method, CMES Comput. Model. Eng. Sci. 5 (6) (2004) 477–496.
[18] S. Bardenhagen, J. Brackbill, D. Sulsky, The material-point method for granular materials, Comput. Methods Appl. Mech. Engrg. 187 (3–4) (2000) 529–541.
[19] J.E. Guilkey, S. Bardenhagen, K. Roessig, J. Brackbill, W. Witzel, J. Foster, Improved contact algorithm for the material point method and application to stress propagation in granular material, CMES Comput. Model. Eng. Sci. 2 (4) (2001) 509–522.
[20] P. Huang, X. Zhang, S. Ma, X. Huang, Contact algorithms for the material point method in impact and penetration simulation, Internat. J. Numer. Methods Engrg. 85 (4) (2011) 498–517.
[21] J.A. Nairn, C.C. Hammerquist, G.D. Smith, New material point method contact algorithms for improved accuracy, large-deformation problems, and proper null-space filtering, Comput. Methods Appl. Mech. Engrg. 362 (2020) 112859.
[22] J.A. Nairn, Modeling heat flow across material interfaces and cracks using the material point method, Comput. Part. Mech. 6 (1) (2019) 133–144.
[23] J. Ma, D. Wang, M. Randolph, A new contact algorithm in the material point method for geotechnical simulations, Int. J. Numer. Anal. Methods Geomech. 38 (11) (2014) 1197–1210.
[24] C. Liu, Q. Sun, G.G. Zhou, Coupling of material point method and discrete element method for granular flows impacting simulations, Internat. J. Numer. Methods Engrg. 115 (2) (2018) 172–188.
[25] J.A. Nairn, Modeling imperfect interfaces in the material point method using multimaterial methods, CMES Comput. Model. Eng. Sci. 1 (1) (2013) 1–15.
[26] Y. Jiang, M. Li, C. Jiang, F. Alonso-Marroquin, A hybrid material-point spheropolygon-element method for solid and granular material interaction, Internat. J. Numer. Methods Engrg. 121 (14) (2020) 3021–3047.
[27] J. Guilkey, R. Lander, L. Bonnell, A hybrid penalty and grid based contact method for the Material Point Method, Comput. Methods Appl. Mech. Engrg. 379 (2021) 113739.
[28] Y. Jiang, Y. Zhao, C.E. Choi, J. Choo, Hybrid continuum–discrete simulation of granular impact dynamics, Acta Geotech. (2022) 1–16.
[29] J.U. Brackbill, H.M. Ruppel, FLIP: A method for adaptively zoned, particle-in-cell calculations of fluid flows in two dimensions, J. Comput. Phys. 65 (2) (1986) 314–343.
[30] F.H. Harlow, The particle-in-cell computing method for fluid dynamics, Methods Comput. Phys. 3 (1964) 319–343.
[31] C.C. Hammerquist, J.A. Nairn, A new method for material point method particle updates that reduces noise and enhances stability, Comput. Methods Appl. Mech. Engrg. 318 (2017) 724–738.
[32] Q.-A. Tran, W. Sołowski, Temporal and null-space filter for the material point method, Internat. J. Numer. Methods Engrg. 120 (3) (2019) 328–360.
[33] P. Menetrey, K. Willam, Triaxial failure criterion for concrete and its generalization, Struct. J. 92 (3) (1995) 311–318.
[34] S. Drucker, W. Prager, Mechanics and plastic analysis or limit design, Q. Appl. Math 2 (52) (1952) 157–165.
[35] C. Liu, W. Sun, ILS-MPM: An implicit level-set-based material point method for frictional particulate contact mechanics of deformable particles, Comput. Methods Appl. Mech. Engrg. 369 (2020) 113168.
[36] E.G. Gilbert, D.W. Johnson, S.S. Keerthi, A fast procedure for computing the distance between complex objects in three-dimensional space, IEEE J. Robot. Autom. 4 (2) (1988) 193–203.
[37] X. Lei, X. Chen, Z. Yang, S. He, L. Zhu, H. Liang, A simple and robust MPM framework for modelling granular flows over complex terrains, Comput. Geotech. 149 (2022) 104867.
[38] S. Bardenhagen, Energy conservation error in the material point method for solid mechanics, J. Comput. Phys. 180 (1) (2002) 383–403.
[39] C.C. Hammerquist, J.A. Nairn, Modeling nanoindentation using the material point method, J. Mater. Res. 33 (10) (2018) 1369–1381.
[40] Q.-A. Tran, W. Sołowski, Generalized interpolation material point method modelling of large deformation problems including strain-rate effects–Application to penetration and progressive failure problems, Comput. Geotech. 106 (2019) 249–265.
[41] E. Susila, R.D. Hryciw, Large displacement FEM modelling of the cone penetration test (CPT) in normally consolidated sand, Int. J. Numer. Anal. Methods Geomech. 27 (7) (2003) 585–602.
[42] J.P. Gray, J.J. Monaghan, R. Swift, SPH elastic dynamics, Comput. Methods Appl. Mech. Engrg. 190 (49–50) (2001) 6641–6662.
[43] K.L. Johnson, K.L. Johnson, Contact Mechanics, Cambridge University Press, 1987.
[44] L. Wang, X. Zhang, Q. Lei, S. Panayides, S. Tinti, A three-dimensional particle finite element model for simulating soil flow with elastoplasticity, Acta Geotech. (2022) 1–15.

[45] E. Yang, H.H. Bui, G.D. Nguyen, C.E. Choi, C.W. Ng, H. De Sterck, A. Bouazza, Numerical investigation of the mechanism of granular flow impact on rigid control structures, Acta Geotech. 16 (8) (2021) 2505–2527.
[46] X. Zhang, E. Oñate, S.A.G. Torres, J. Bleyer, K. Krabbenhoft, A unified Lagrangian formulation for solid and fluid dynamics and its possibility for modelling submarine landslides and their consequences, Comput. Methods Appl. Mech. Engrg. 343 (2019) 314–338.
[47] K. Liao, C. Hu, M. Sueyoshi, Free surface flow impacting on an elastic structure: Experiment versus numerical simulation, Appl. Ocean Res. 50 (2015) 192–208.
[48] J.J. Monaghan, Simulating free surface flows with SPH, J. Comput. Phys. 110 (2) (1994) 399–406.
[49] L. Cueto-Felgueroso, I. Colominas, G. Mosqueira, F. Navarrina, M. Casteleiro, On the Galerkin formulation of the smoothed particle hydrodynamics method, Internat. J. Numer. Methods Engrg. 60 (9) (2004) 1475–1512.